www.czasopisma.pan.pl PAN POLSKA AKADEMIA NAUK www.journals.pan.pl

Arch. Min. Sci. **70** (2025), 1, 115-145

Electronic version (in color) of this paper is available: http://mining.archives.pl

DOI: https://doi.org/10.24425/ams.2025.154166

WENJIA LU[1], YIMIN ZHANG[1*], ZUNLING DU[1], WEIBO HUANG[1]

RESEARCH ON MECHATRONICS INTEGRATION MODELLING AND COUPLED DYNAMIC CHARACTERISTICS IN A SHEARER CUTTING SECTION GEARBOX

The time-varying mesh stiffness (TVMS) and static transmission error (STE) are the main dynamic load excitation forms in the shearer cutting section gearbox (SCSG). The gearbox comprises two-stage planetary gear sets and multi-stage parallel gear sets. The structure of the multi-stage transmission and its rich internal dynamic excitation result in unique and complex dynamic behavior. In this paper, a coupled mechatronic integration dynamic model for SCSG and motor is developed, in which the multi-stage coupling excitation effects caused by gear mesh stiffness and static transmission error are fully simulated, thereby clarifying the interaction mechanism between the motor and transmission system. Based on the simulation model, the dynamic load characteristics of the SCSG are studied. The results show that load-sharing performance is improved with the increases of drum torque in the planetary gear sets (PGSs), which indicates that the load-sharing performance of the planetary gears can be effectively guaranteed in the process of increasing the coal mining rate. Through the combination of numerical simulation and experimental research, it is verified that the simulated signals are consistent with the experimental data for motor current. Meanwhile, relying on the proposed mechatronics model, extensive vibration information of the gearbox can be identified through the stator current signal. These results reference the vibration response analysis and signal monitoring of complex transmission systems.

Keywords: Longwall shearer; Planetary gear sets; Mechatronics model; Static transmission error; Dynamic characteristics; Load sharing performance

1. Introduction

Coal is one of the main sources of energy. The double-drum shearers are mechanised equipment suitable for longwall coal mining. Its continuous and efficient working characteristics make it a broad application market and prospect in coal mining. The shearer-cutting section is the direct

1 ZHAOQING UNIVERSITY, COLLEGE OF MECHANICAL AND AUTOMOTIVE ENGINEERING, ZHAOQING, CHINA

* Corresponding author: zhangyimin@zqu.edu.cn

operation mechanism of coal mining, and it is in harsh conditions of heavy load and impact for a long time. The research on its dynamic characteristics is of great significance to the working life of shearers and the efficiency of coal mining. Shearer cutting section gearbox (SCSG) is a complex transmission system consisting of two-stage planetary gear sets (PGSs) and multi-stage parallel gear sets. Time-varying mesh stiffness (TVMS) and static transmission error (STE) are typical forms of internal excitation in gear transmission systems. During the meshing transmission process between the planet and sun, as well as the planet and ring, complex dynamic behaviours will be generated because of these excitation effects in the PGSs. At the same time, each stage meshing transmission of gear pairs in parallel gear sets would also produce vibration and noise with different amplitudes due to these internal excitations. When these dynamic responses are coupled and superimposed among various stages of the transmission system, extremely complex multi-source coupled dynamic behaviours are formed inside the SCSG.

Nomenclature

c_{jpn} – mesh damping between central gears and planets ($j = r, s$)
c_{jx}, c_{jy} – bearing damping of central members ($j = c, r, s$)
c_p – bearing damping of planets
c_{ju} – torsional damping of central members ($j = c, r, s$)
c_{ISl} – coupling damping of intermediate shafts at each stage ($l = 1, 2, 3$)
c_{HS} – coupling damping of high-speed shaft
$c_{i,i+1}$ – mesh damping of parallel gear pairs
c_{rox}, c_{roy} – bearing damping of the rotor
$\boldsymbol{C}_b$, $\boldsymbol{C}_m(t)$ – bearing damping matrix and mesh damping matrix of the system
$e_{i,i+1}$ – static transmission error of parallel gear pairs
e_{jpn} – static transmission error between central gears and planets ($j = r, s$)
f_{n1}, f_{n2} – mesh frequency of the first and second stage parallel gear sets
f_{m3}, f_{m4} – mesh frequency of the third and fourth stage planetary gear sets
f_e – power supply frequency
$\boldsymbol{F}(t)$ – internal excitation vector of the system
G_i – multistage parallel gear ($i = 1, 2, \ldots, 8$)
GB_i – bearings for multi-tage parallel gear ($i = 1, 2, \ldots, 8$)
I_j – moment of inertia for central members and planets ($j = c, r, s, p$)
I_{ro} – rotor inertia
$\boldsymbol{I}(t)$ – stator and rotor current vector
k_{jpn} – mesh stiffness between central gears and planets ($j = r, s$)
k_{jx}, k_{jy} – bearing stiffness of central members ($j = c, r, s$)
k_p – bearing stiffness of planets
k_{ju} – torsional stiffness of central members ($j = c, r, s$)
$k_{i,i+1}$ – mesh stiffness of parallel gear pairs
k_{rox}, k_{roy} – bearing stiffness of the rotor
k_{HS} – coupling stiffness of high-speed shaft
k_{ISl} – coupling stiffness of the intermediate shafts at each stage ($l = 1, 2, 3$)
$\boldsymbol{K}_{i,i+1}$ – meshing stiffness matrix of parallel gear sets

$\boldsymbol{K}_b$, $\boldsymbol{K}_m(t)$ – bearing stiffness matrix and meshing stiffness matrix of the system
$\boldsymbol{K}_{IS1}$, $\boldsymbol{K}_{IS2}$, $\boldsymbol{K}_{IS3}$ – coupling stiffness matrix between each stage transmission system
L_{st}, L_{ro} – synchronous inductance of stator and rotor
L_m – magnetizing inductance
m_j – mass of central members and planets ($j = c, r, s, p$)
m_{ro} – rotor mass
$\boldsymbol{M}$ – mass matrix of the system
n_p – motor pole pairs
N – number of planet gears
$\boldsymbol{q}$ – generalized displacement vector of the system
r_j – base radius of central members and planets ($j = c, r, s, p$)
R_{st}, R_{ro} – stator and rotor resistance
T_j – external torque acting on the centre gear ($j = r, s$)
T_e – electromagnetic torque
$\boldsymbol{T}$ – external torque vector of the system
$\boldsymbol{U}(t)$ – stator supply voltage vector
v_q – traction speed of the shearer
α_j – pressure angle of central gears ($j = r, s$)
ω – synchronous angular velocity of the rotor
ω_{ro} – mechanical angular velocity of the rotor
ψ_n – position angle of the nth planet
$\psi_{i,i+1}$ – angle between the mesh line and y axis for parallel gear pairs

Subscripts

c, r, s – carrier, ring, sun
p – planet
n – planet number
u – equivalent torsion direction
st, ro – stator and rotor of the motor
d, q – synchronous rotation coordinate axis
$i,i+1$ – parallel gear pair number ($i = 1, 2, 4, 5, 6, 7$)
x, y – horizontal and vertical translation directions
ζ, η – translation direction of planets in the following coordinate system

The PGSs are the main reduction mechanism in the SCSG. Because of the compact structure and numerous components, the modelling method and dynamic behaviour of the PGSs are worthy of special attention and research. For the study of the relationship between error excitation and the dynamic behaviour of PGSs, Kahraman [1,2] developed a three-dimensional universal model to simulate the dynamic behaviour of a single-stage helical planetary gear set, and derived a periodic excitation function based on mesh stiffness and static transmission error (STE), these parameters are assumed to be known from static elastic analysis. This model has important reference values for dynamic excitation mode study, load-sharing behaviour and the influence of the meshing phase on the system. Inalpolat and Kahraman [3,4] proposed a nonlinear time-varying dynamic model that includes periodic TVMS and pitch correlation to predict the modulation

sidebands of PGSs. They account for amplitude modulation (AM) caused by the rotation of the planet carrier to simulate the acceleration spectrum at a fixed position in the planetary gearbox housing. They continued to systematically research the impact of manufacturing errors on the dynamic characteristics, gear stress, and planetary load-sharing behaviour in the PGSs.

The mesh stiffness of PGSs varies with the number of contact tooth pairs in gear rotation. Bahk and Parker [5] studied the nonlinear dynamic behaviour of planetary gears in the range of meaningful meshing frequency by numerical and analytical methods, to solve the stability boundary problem of PGSs caused by time-varying meshing stiffness excitation. Sheng et al. [6] proposed a nonlinear transverse and torsional coupling dynamic model for PGSs that considers the effects of eccentricity error, static transmission error (STE), and time-varying meshing stiffness (TVMS). This study expands the current understanding of the dynamic load-sharing behaviour for planetary gear systems and provides a reference for the design of PGSs. Cao et al. [7] pointed out that the presence of gear eccentricity error would change the centre distance and mesh position of the gear pair, which would directly affect the mesh stiffness. Based on this, the dynamic model of PGSs was developed with sun or planet eccentricity. In this study, a new idea is proposed regarding the interaction mechanism between error and stiffness excitation of PGSs. If the planets are not in the same relative mesh position at any time, the uneven load distribution between the planets will be affected by the mesh stiffness. Pedrero et al. [8] established the conditions for the uneven load distribution between the planets due to mesh stiffness and proposed a calculation method considering the corresponding influencing factors. These studies all show that the TVMS excitations of PGSs have an important effect on the dynamic behaviour of each planet, such as load-sharing behaviour and dynamic force level, etc.

The study of multi-stage PGSs is based on the single-stage dynamic model. The literature [9,10] considered the influence of axial deformation, gyroscopic effect, TVMS and inter-stage coupling of components, and a lumped mass model was established for two-stage PGSs. The vibration modes and load-sharing characteristics of multistage PGSs are analyzed. The literature [11,12] proposed a coupled bent-torsional vibration model of multi-stage PGSs and studied the effects of eccentricity error, tooth thickness error, pitch error and carrier assembly error on the dynamic characteristics and load-sharing performance. Hammami et al. [13,14] developed a dynamic model for back-to-back two-stage PGSs and analysed the influence of the mesh stiffness and load variation on the load-sharing performance of the PGSs during starting, braking and shifting. Subsequently, Mbarek et al. [15] conducted a comparative analysis of experimental and operational modes for the back-back two-stage PGSs. In this study, both experimental and operational modal analyses are effectively applied to the multi-stage PGSs, revealing the essence of its dynamic characteristics during variable speed conditions. The above research analysed the coupling dynamic modelling method, internal excitation form and load-sharing performance of multi-stage PGSs, which provides a reference for the study of the dynamic behaviour of SCSG in this paper.

The power source for the SCSG is the asynchronous motor drive. The study of the dynamic behaviour of motor and multistage gear coupling systems is of great significance for clarifying the interaction between mechanical and electrical systems and exploring the influence of motors on mechanical transmission systems. From the perspective of optimising system dynamic force, a dynamic model of an electromechanical drive system, including a vector control unit, was established by Mężyk [16,17]. Then Świtoński and Mężyk [18] conducted parameter selection through sensitivity analysis for optimising the dynamic properties of the electromechanical drive system. On this basis, Mężyk et al. [19] proposed a new concept of SCSG, which directly connects an electronically controlled permanent magnet motor with a cutter head mechanical

system. An electromechanical model was established to determine electrical parameters in the cutting process, and the interaction between electrical and mechanical subsystems was explored. Based on the electromechanical model, Bai and Qin et al. [20,21] fully considered the effects of external excitations, such as voltage transient and internal excitations and time-varying meshing stiffness and damping. The study found that voltage transients can have a significant impact on the dynamic characteristics of electromechanical systems, and thus proposed reasonable suggestions to improve their stability. They also studied the electromechanical coupling problem caused by the interaction between the motor and gear system. They predicted an effective method for detecting asymmetric voltage sag conditions through frequency analysis of the electromechanical system. The research on electromechanical systems mainly focuses on the interaction relationship between mechanical and electrical systems, and the impact of motors on transmission systems. Furthermore, outstanding achievements have been made in selecting design parameters, optimising dynamic performance and improving the stability of the electromechanical coupling system.

In summary, scholars have carried out a lot of in-depth research on planetary gear dynamics and the mechatronics model of motor gearbox, which provides a reference for the dynamic analysis of the multi-stage gear transmission system of SCSG. At present, little attention is paid to the influence of internal dynamic excitations such as TVMS and STE, so it is difficult to comprehensively obtain complex vibration information inside the SCSG. This paper intends to develop a coupled dynamic model with two-stage planetary gear sets and multi-stage parallel gear sets in the SCSG. The dynamic model will simulate the multi-stage coupling excitation effects caused by the TVMS and STE. It will also explore the interaction mechanisms between the motor and the transmission system. Additionally, using the electromechanical coupling model, the study will identify vibration information within the SCSG through motor current signature analysis.

2. Coupled dynamic model of the SCSG

This paper takes the cutting section of the shearer as the research object, as shown in Fig. 1, which is a complex electromechanical system composed of the motor, multi-stage parallel gear sets and two-stage PGSs. This section mainly establishes the lumped mass model of planetary gear sets, parallel gear sets and the dynamic model of asynchronous motor, where the dynamic

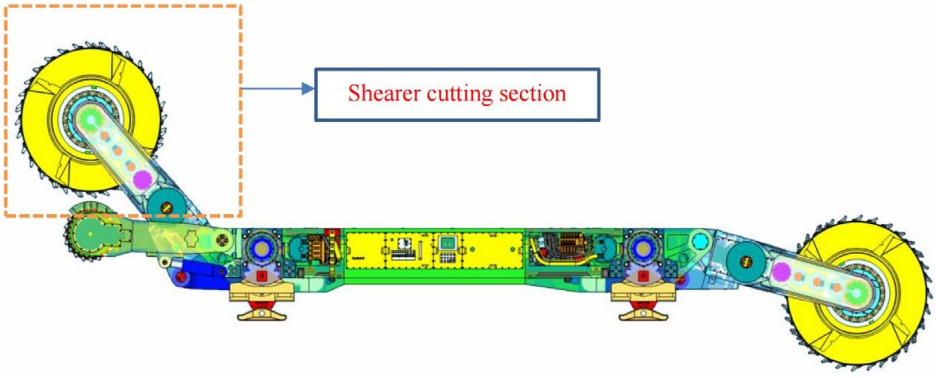

Fig. 1. Three dimensional model of the shearer cutting section

model of PGSs proposed by Lin and Parker [22] is adopted, the lumped mass model of multi-stage parallel gear sets is adopted from Zhang et al. [23], and the asynchronous motor model is established based on the equivalent motor model proposed by Kron [24]. Finally, a coupled dynamic model of the SCSG is developed through the connection relationship between different stages.

The simplified dynamic model of the SCSG is shown in Fig. 2, which is divided into input-stage motor, first-stage parallel gear set, second-stage parallel gear set, third-stage planetary gear set, fourth-stage planetary gear set and output-stage drum. In Fig. 2, the gear (G_1) of the first-stage parallel gear set is connected to the motor rotor through an input shaft, which is defined as the high-speed shaft (HSS). The gear (G_3) of the first-stage parallel gear set is connected to the gear (G_4) of the second-stage parallel gear set, and the connecting shaft is called the first intermediate speed shaft (ISS_1). The gear ($G8$) of the second-stage parallel gear set and the sun (S_3) of the third-stage PGS are coupled through the second intermediate speed shaft (ISS_2). The third-stage carrier (C_3) is connected to the fourth-stage sun gear (S_4) through the third intermediate speed shaft (ISS_3). The cutting drum of the shearer is connected to the fourth-stage carrier (C_4), and the output shaft is defined as the low-speed shaft (LSS).

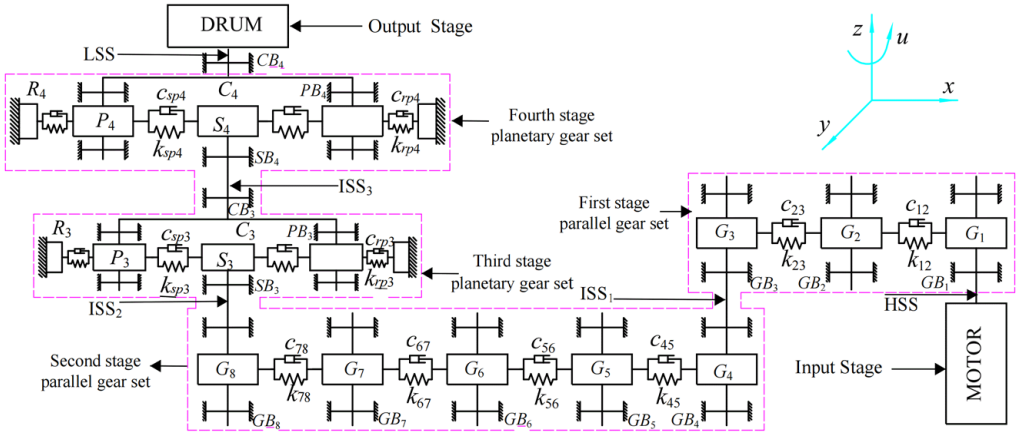

Fig. 2. Dynamic model of the shearer cutting section gearbox (SCSG)

2.1. Dynamic model of multi-stage gear transmission system

The multi-stage gear transmission system of the shearer cutting section includes multi-stage parallel gear sets and two-stage planetary gear sets. The dynamic model of single-stage PGS is illustrated in Fig. 3, which was built based on the literature [4,22].

The principal coordinate system (Ox_jy_j, $j = c, r, s$) and the follow-up coordinate system ($O_n\zeta_n\eta_n$) are established, respectively. The origin O of the principal coordinate is located in the geometric center of the central members, and the axis x_j ($j = c, r, s$) is located at point O and center point of the first planet gear. The follow-up coordinate system is fixed with the carrier and rotates at the same angular velocity, in which its origin is located at the theoretical center of the nth planet gear. In this model, the planetary system is simplified into different lumped mass points, the mesh action between gears is simulated by spring-damping along the direction

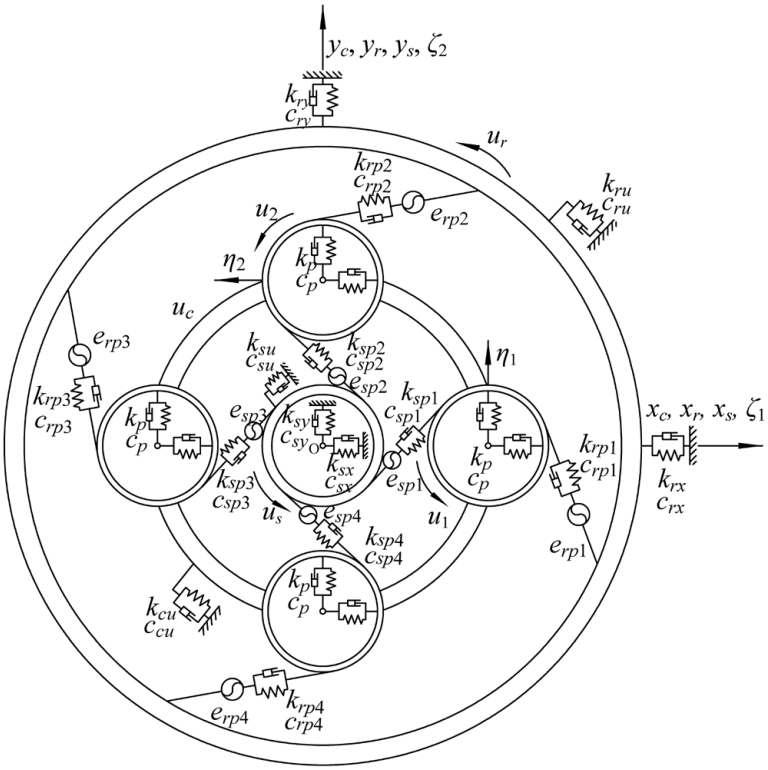

Fig. 3. Dynamic model of single-stage PGS

of the meshing line, and the bearings are modeled by linear spring and damping. The rotational coordinates are $u_j = \theta_j r_j$, $j = c, r, s, 1, 2, \ldots, N$, where θ_j is the component rotation angle, r_j is the base circle radius for the sun, ring and planet, and the radius of the circle passing through the planet centers for the carrier.

The dynamic model of the parallel gear sets is shown in Fig. 4, and it is consistent with the model proposed by Zhang et al. [23]. In which k_{ix}, k_{iy} and k_{jx}, k_{jy} represent the bearing stiffness of parallel gear sets in x and y directions, c_{ix}, c_{iy} and c_{jx}, c_{jy} represent the bearing damping of parallel gear sets in x and y directions. k_{iu}, k_{ju} and c_{iu}, c_{ju} represent the torsional stiffness and damping of parallel gear sets. As shown in Fig. 4, the mesh stiffness and bearing stiffness are simulated by the spring-damping system. The translational displacements are expressed as x, y, and the torsional displacement is defined as $u = r\theta$. r_i, r_j represent the base circle radius for the gear set.

The dynamic mesh force of the gear pair in the PGS can be defined as:

$$F_{jpn}(t) = c_{jpn}\dot{\delta}_{jpn}(t) + k_{jpn}\delta_{jpn}(t) \tag{1a}$$

Where $\delta_{jpn}(t)$ is the relative displacement along the line of action for the gear pair, given as follows:

$$\delta_{jpn}(t) = -x_j(t)\sin\psi_{jn} + y_j(t)\cos\psi_{jn} - \lambda\zeta_n(t)\sin\alpha_j - \eta_n(t)\cos\alpha_j + u_j(t) + \lambda u_n(t) + e_{jpn}(t) \tag{1b}$$

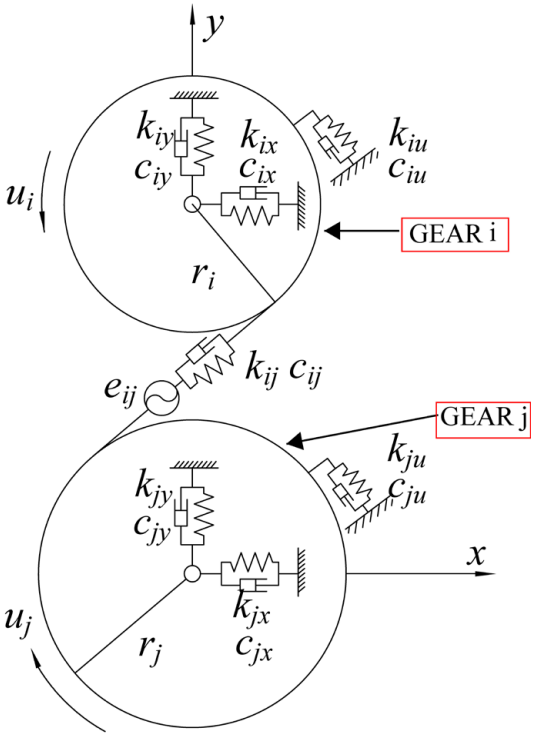

Fig. 4. Dynamic model of parallel gear set

The differential equation of motion for the central gears can be expressed as:

$$m_j \ddot{x}_j(t) - \sum_{n=1}^{N} F_{jpn}(t) \sin\psi_{jn} + k_{jx} x_j(t) + c_{jx} \dot{x}_j(t) = 0 \tag{2a}$$

$$m_j \ddot{y}_j(t) + \sum_{n=1}^{N} F_{jpn}(t) \cos\psi_{jn} + k_{jy} y_j(t) + c_{jy} \dot{y}_j(t) = 0 \tag{2b}$$

$$(I_j / r_j^2)\ddot{u}_j(t) - \sum_{n=1}^{N} F_{jpn}(t) + k_{ju} u_j(t) + c_{ju} \dot{u}_j(t) = T_j / r_j \tag{2c}$$

In these equations, when $j = s$ (external $s - pn$ gear pair), $\lambda = 1$; when $j = r$ (internal $r - pn$ gear pair), $\lambda = -1$. $\psi_{jn} = \psi_n - \alpha_j$, where α_j denotes the pressure angle of the gear, T_j denotes the external torque acting on the center gear.

The differential equation of motion for planet gears can be written as:

$$m_{pn} \ddot{\zeta}_n(t) - F_{spn}(t) \sin\alpha_s - F_{rpn}(t) \sin\alpha_r - k_p \delta_{pn\zeta}(t) - c_p \dot{\delta}_{pn\zeta}(t) = 0 \tag{3a}$$

$$m_{pn} \ddot{\eta}_n(t) - F_{spn}(t) \cos\alpha_s - F_{rpn}(t) \cos\alpha_r - k_p \delta_{pn\eta}(t) - c_p \dot{\delta}_{pn\eta}(t) = 0 \tag{3b}$$

$$(I_{pn}/(r_{pn}^2)^2)\ddot{u}_{pn}(t) - F_{spn}(t) + F_{rpn}(t) = 0 \tag{3c}$$

Where $\delta_{pn\zeta}(t)$ and $\delta_{pn\eta}(t)$ are the relative displacements between the carrier and the nth planet in the follow-up coordinate system, given as follows:

$$\delta_{pn\zeta}(t) = x_c(t)\cos\psi_n + y_c(t)\sin\psi_n - \zeta_n(t) \tag{3d}$$

$$\delta_{pn\eta}(t) = -x_c(t)\sin\psi_n + y_c(t)\cos\psi_n - \eta_n(t) + u_c(t) \tag{3e}$$

The differential equation of the motion for the carrier can be expressed as:

$$m_c\ddot{x}_c(t) + \sum_{n=1}^{N}\begin{bmatrix} k_p(\delta_{pn\zeta}(t)\cos\psi_n - \delta_{pn\eta}(t)\sin\psi_n) + \\ + c_p(\dot{\delta}_{pn\zeta}(t)\cos\psi_n - \dot{\delta}_{pn\eta}(t)\sin\psi_n) \end{bmatrix} + k_{cx}x_c(t) + c_{cx}\dot{x}_c(t) = 0 \tag{4a}$$

$$m_c\ddot{y}_c(t) + \sum_{n=1}^{N}\begin{bmatrix} k_p(\delta_{pn\zeta}(t)\sin\psi_n + \delta_{pn\eta}(t)\cos\psi_n) + \\ + c_p(\dot{\delta}_{pn\zeta}(t)\sin\psi_n + \dot{\delta}_{pn\eta}(t)\cos\psi_n) \end{bmatrix} + k_{cy}y_c(t) + c_{cy}\dot{y}_c(t) = 0 \tag{4b}$$

$$(I_c/r_c^2)\ddot{u}_c(t) + \sum_{n=1}^{N}k_p\delta_{pn\eta}(t) + \sum_{n=1}^{N}c_p\dot{\delta}_{pn\eta}(t) + k_{cu}u_c(t) + c_{cu}\dot{u}_c(t) = 0 \tag{4c}$$

The motion equations for the parallel gear sets can be written similarly Reference [23].

2.2. Mathematical model of the motors

Park [24] proposed a two-phase equivalent motor model from the perspective of coordinate transformation, which greatly reduced the difficulty of solving the dynamic problem of asynchronous motors. The coordinate transformation method proposed by Park [24] is applied to transform the mathematical model for asynchronous motors in three-phase stationary coordinates into two-phase synchronous rotating coordinates.

The basic equations of the dynamic model for asynchronous motors are voltage balance equations and rotor motion differential equations. The voltage equation with current as the state variable is described as [24]:

$$\boldsymbol{U}(t) = \boldsymbol{A}\boldsymbol{I}(t) + \boldsymbol{B}\frac{d}{dt}[\boldsymbol{I}(t)] \tag{5}$$

Where $\boldsymbol{U}(t) = [u_{dst}, u_{qst}, 0, 0]^{\mathrm{T}}$ denotes the stator supply voltage vector, $\boldsymbol{I}(t) = [i_{dst}, i_{qst}, i_{dro}, i_{qro}]^T$ denotes the stator and rotor current vector.

The coefficient matrices $\boldsymbol{A}$ and $\boldsymbol{B}$ in formula (5) can be expressed as:

$$\boldsymbol{A} = \begin{bmatrix} R_{st} & -\omega L_{st} & 0 & -\omega L_m \\ \omega L_{st} & R_{st} & \omega L_m & 0 \\ 0 & -(\omega-\omega_{ro})L_m & R_{ro} & -(\omega-\omega_{ro})L_{ro} \\ (\omega-\omega_{ro})L_m & 0 & (\omega-\omega_{ro})L_{ro} & R_{ro} \end{bmatrix} \tag{6a}$$

$$\boldsymbol{B}=\begin{bmatrix} L_{st} & 0 & L_m & 0 \\ 0 & L_{st} & 0 & L_m \\ L_m & 0 & L_{ro} & 0 \\ 0 & L_m & 0 & L_{ro} \end{bmatrix} \tag{6b}$$

The electromagnetic torque equation for the motor can be written as:

$$T_e = n_p L_m (i_{stq} i_{rod} - i_{std} i_{roq}) \tag{7}$$

As shown in Fig. 2, the motor rotor (*ro*) is connected to the gear (G_1) in a parallel gear set through HSS. The coupling stiffness and coupling damping are defined as k_{HS} and c_{HS} respectively, so the differential equation of motion for the rotor can be expressed as:

$$\begin{cases} m_{ro}\ddot{x}_{ro} + k_{rox}x_{ro} + c_{rox}\dot{x}_{ro} - k_{HSx}(x_{ro} - x_1) - c_{HSx}(\dot{x}_{ro} - \dot{x}_1) = 0 \\ m_{ro}\ddot{y}_{ro} + k_{roy}y_{ro} + c_{roy}\dot{y}_{ro} - k_{HSy}(y_{ro} - y_1) - c_{HSy}(\dot{y}_{ro} - \dot{y}_1) = 0 \\ (I_{ro} / {r_{ro}}^2)\ddot{u}_{ro} - k_{HSu}(u_{ro} - u_1) - c_{HSu}(\dot{u}_{ro} - \dot{u}_1) = T_e / r_{ro} \end{cases} \tag{8}$$

2.3. Assembly of the stages for the SCSG

According to the position of the coupling shaft in the gearbox, the inter-stage assembly method in References [25,26] is adopted to assemble various structures for the SCSG. The coupling stiffness matrix of intermediate shafts can be uniformly defined as:

$$\boldsymbol{K}_{ISl} = \begin{bmatrix} k_{ISlx} & 0 & 0 \\ 0 & k_{ISly} & 0 \\ 0 & 0 & k_{ISlu} \end{bmatrix} \quad (l = 1,\ 2,\ 3) \tag{9}$$

The first-stage gear (G_3) is coupled with the second-stage gear (G_4) through ISS_1, so the assembly of the two stages stiffness matrix can be expressed as:

$$\boldsymbol{K}_{cp}^{12} = \begin{bmatrix} \boldsymbol{K}_{12} & -\boldsymbol{K}_{12} & \boldsymbol{0} & \boldsymbol{0} & \boldsymbol{0} & \boldsymbol{0} & \boldsymbol{0} & \boldsymbol{0} \\ -\boldsymbol{K}_{12} & \boldsymbol{K}_{12}+\boldsymbol{K}_{23} & -\boldsymbol{K}_{23} & \boldsymbol{0} & \boldsymbol{0} & \boldsymbol{0} & \boldsymbol{0} & \boldsymbol{0} \\ \boldsymbol{0} & -\boldsymbol{K}_{23} & \boldsymbol{K}_{23}+\boldsymbol{K}_{IS1} & -\boldsymbol{K}_{IS1} & \boldsymbol{0} & \boldsymbol{0} & \boldsymbol{0} & \boldsymbol{0} \\ \boldsymbol{0} & \boldsymbol{0} & -\boldsymbol{K}_{IS1} & \boldsymbol{K}_{IS1}+\boldsymbol{K}_{45} & -\boldsymbol{K}_{45} & \boldsymbol{0} & \boldsymbol{0} & \boldsymbol{0} \\ \boldsymbol{0} & \boldsymbol{0} & \boldsymbol{0} & -\boldsymbol{K}_{45} & \boldsymbol{K}_{45}+\boldsymbol{K}_{56} & -\boldsymbol{K}_{56} & \boldsymbol{0} & \boldsymbol{0} \\ \boldsymbol{0} & \boldsymbol{0} & \boldsymbol{0} & \boldsymbol{0} & -\boldsymbol{K}_{56} & \boldsymbol{K}_{56}+\boldsymbol{K}_{67} & -\boldsymbol{K}_{67} & \boldsymbol{0} \\ \boldsymbol{0} & \boldsymbol{0} & \boldsymbol{0} & \boldsymbol{0} & \boldsymbol{0} & -\boldsymbol{K}_{67} & \boldsymbol{K}_{67}+\boldsymbol{K}_{78} & -\boldsymbol{K}_{78} \\ \boldsymbol{0} & \boldsymbol{0} & \boldsymbol{0} & \boldsymbol{0} & \boldsymbol{0} & \boldsymbol{0} & -\boldsymbol{K}_{78} & \boldsymbol{K}_{78} \end{bmatrix} \tag{10}$$

The second-stage gear (G_8) is coupled with the third-stage sun through ISS_2, so the assembly of two stages stiffness matrix can be expressed as:

$$\boldsymbol{K}_{cp}^{23}=\begin{bmatrix}
\boldsymbol{K}_{45} & -\boldsymbol{K}_{45} & 0 & 0 & 0 & 0 & 0 & 0 & 0 & 0 & 0 \\
-\boldsymbol{K}_{45} & \boldsymbol{K}_{45}+\boldsymbol{K}_{56} & -\boldsymbol{K}_{56} & 0 & 0 & 0 & 0 & 0 & 0 & 0 & 0 \\
0 & -\boldsymbol{K}_{56} & \boldsymbol{K}_{56}+\boldsymbol{K}_{67} & -\boldsymbol{K}_{67} & 0 & 0 & 0 & 0 & 0 & 0 & 0 \\
0 & 0 & -\boldsymbol{K}_{67} & \boldsymbol{K}_{67}+\boldsymbol{K}_{78} & -\boldsymbol{K}_{78} & 0 & 0 & 0 & 0 & 0 & 0 \\
0 & 0 & 0 & -\boldsymbol{K}_{78} & \boldsymbol{K}_{78}+\boldsymbol{K}_{IS2} & 0 & 0 & -\boldsymbol{K}_{IS2} & 0 & 0 & 0 \\
0 & 0 & 0 & 0 & 0 & \sum \boldsymbol{K}_{c1}^{n(3)} & 0 & 0 & \boldsymbol{K}_{c2}^{1(3)} & \cdots & \boldsymbol{K}_{c2}^{N(3)} \\
0 & 0 & 0 & 0 & 0 & 0 & \sum \boldsymbol{K}_{r1}^{n(3)} & 0 & \boldsymbol{K}_{r2}^{1(3)} & \cdots & \boldsymbol{K}_{r2}^{N(3)} \\
0 & 0 & 0 & 0 & -\boldsymbol{K}_{IS2} & 0 & 0 & \sum \boldsymbol{K}_{s1}^{n(3)}+\boldsymbol{K}_{IS2} & \boldsymbol{K}_{s2}^{1(3)} & \cdots & \boldsymbol{K}_{s2}^{N(3)} \\
0 & 0 & 0 & 0 & 0 & \boldsymbol{K}_{c2}^{1(3)} & \boldsymbol{K}_{r2}^{1(3)} & \boldsymbol{K}_{s2}^{1(3)} & \boldsymbol{K}_{pp}^{1(3)} & 0 & 0 \\
0 & 0 & 0 & 0 & 0 & \vdots & \vdots & \vdots & 0 & \ddots & 0 \\
0 & 0 & 0 & 0 & 0 & \boldsymbol{K}_{c2}^{N(3)} & \boldsymbol{K}_{r2}^{N(3)} & \boldsymbol{K}_{s2}^{N(3)} & 0 & 0 & \boldsymbol{K}_{pp}^{N(3)}
\end{bmatrix} \tag{11}$$

The third-stage carrier is coupled with the fourth-stage sun through ISS_3, so the assembly of the two stages stiffness matrix can be expressed as:

$$\boldsymbol{K}_{cp}^{34}=\begin{bmatrix}
\sum \boldsymbol{K}_{c1}^{n(3)}+\boldsymbol{K}_{IS3} & 0 & 0 & \boldsymbol{K}_{c2}^{1(3)} & \cdots & \boldsymbol{K}_{c2}^{N(3)} & 0 & 0 & -\boldsymbol{K}_{IS3} & 0 & 0 & 0 \\
0 & \sum \boldsymbol{K}_{r1}^{n(3)} & 0 & \boldsymbol{K}_{r2}^{1(3)} & \cdots & \boldsymbol{K}_{r2}^{N(3)} & 0 & 0 & 0 & 0 & 0 & 0 \\
0 & 0 & \sum \boldsymbol{K}_{s1}^{n(3)} & \boldsymbol{K}_{s2}^{1(3)} & \cdots & \boldsymbol{K}_{s2}^{N(3)} & 0 & 0 & 0 & 0 & 0 & 0 \\
\boldsymbol{K}_{c2}^{1(3)} & \boldsymbol{K}_{r2}^{1(3)} & \boldsymbol{K}_{s2}^{1(3)} & \boldsymbol{K}_{pp}^{1(3)} & 0 & 0 & 0 & 0 & 0 & 0 & 0 & 0 \\
\vdots & \vdots & \vdots & 0 & \ddots & 0 & 0 & 0 & 0 & 0 & 0 & 0 \\
\boldsymbol{K}_{c2}^{N(3)} & \boldsymbol{K}_{r2}^{N(3)} & \boldsymbol{K}_{s2}^{N(3)} & 0 & 0 & \boldsymbol{K}_{pp}^{N(3)} & 0 & 0 & 0 & 0 & 0 & 0 \\
0 & 0 & 0 & 0 & 0 & 0 & \sum \boldsymbol{K}_{c1}^{n(4)} & 0 & 0 & \boldsymbol{K}_{c2}^{1(4)} & \cdots & \boldsymbol{K}_{c2}^{N(4)} \\
0 & 0 & 0 & 0 & 0 & 0 & 0 & \sum \boldsymbol{K}_{r1}^{n(4)} & 0 & \boldsymbol{K}_{r2}^{1(4)} & \cdots & \boldsymbol{K}_{r2}^{N(4)} \\
-\boldsymbol{K}_{IS3} & 0 & 0 & 0 & 0 & 0 & 0 & 0 & \sum \boldsymbol{K}_{s1}^{n(4)}+\boldsymbol{K}_{IS3} & \boldsymbol{K}_{s2}^{1(4)} & \cdots & \boldsymbol{K}_{s2}^{N(4)} \\
0 & 0 & 0 & 0 & 0 & 0 & \boldsymbol{K}_{c2}^{1(4)} & \boldsymbol{K}_{r2}^{1(4)} & \boldsymbol{K}_{s2}^{1(4)} & \boldsymbol{K}_{pp}^{1(4)} & 0 & 0 \\
0 & 0 & 0 & 0 & 0 & 0 & \vdots & \vdots & \vdots & 0 & \ddots & 0 \\
0 & 0 & 0 & 0 & 0 & 0 & \boldsymbol{K}_{c2}^{N(4)} & \boldsymbol{K}_{r2}^{N(4)} & \boldsymbol{K}_{s2}^{N(4)} & 0 & 0 & \boldsymbol{K}_{pp}^{N(4)}
\end{bmatrix} \tag{12}$$

In formulas (10)-(12), $\boldsymbol{K}_{IS1}$, $\boldsymbol{K}_{IS2}$ and $\boldsymbol{K}_{IS3}$ represent the coupling stiffness matrices among different stages, and their specific forms are defined by formula (9). The mesh stiffness matrices for the parallel gear sets adopted in formulas (10) and (11) can be obtained by Reference [27,28]. The matrices used in formula (12) can be found in Reference [22].

After inter-stage assembly, the motion differential equation of the system can be expressed as:

$$\boldsymbol{M}\ddot{\boldsymbol{q}}(t)+(\boldsymbol{C}_b+\boldsymbol{C}_m(t))\dot{\boldsymbol{q}}(t)+(\boldsymbol{K}_b+\boldsymbol{K}_m(t))\boldsymbol{q}(t)=\boldsymbol{T}+\boldsymbol{F}(t) \tag{13}$$

Where the bearing stiffness matrix $\boldsymbol{K}_b$, bearing damping matrix $\boldsymbol{C}_b$, and mesh damping matrix $\boldsymbol{C}_m(t)$ can be found in Reference [28]. The mesh stiffness matrix $\boldsymbol{K}_m(t)$ of the system is obtained by the assembly of inter-stage stiffness matrices.

The generalised displacement vector, external torque vector and transmission error excitation vector of the system can be defined as:

$$\boldsymbol{q}(t)=\left(\begin{array}{l}\underbrace{\overbrace{x_r,y_r,u_r}^{\text{rotor}},\overbrace{x_1,y_1,u_1}^{G_1},\overbrace{x_2,y_2,u_2}^{G_2},\overbrace{x_3,y_3,u_3}^{G_3}}_{\text{first stage}}\\ \underbrace{\overbrace{x_4,y_4,u_4}^{G_4},\overbrace{x_5,y_5,u_5}^{G_5},\overbrace{x_6,y_6,u_6}^{G_6},\overbrace{x_7,y_7,u_7}^{G_7},\overbrace{x_8,y_8,u_8}^{G_8}}_{\text{second stage}}\\ \underbrace{\overbrace{x_c^{(3)},y_c^{(3)},u_c^{(3)}}^{\text{carrier}},\overbrace{x_r^{(3)},y_r^{(3)},u_r^{(3)}}^{\text{ring}},\overbrace{x_s^{(3)},y_s^{(3)},u_s^{(3)}}^{\text{sun}},\overbrace{\zeta_{p1}^{(3)},\eta_{p1}^{(3)},u_{p1}^{(3)}}^{\text{planet-1}},\cdots,\overbrace{\zeta_{pn}^{(3)},\eta_{pn}^{(3)},u_{pn}^{(3)}}^{\text{planet-n}}}_{\text{third stage}}\\ \underbrace{\overbrace{x_c^{(4)},y_c^{(4)},u_c^{(4)}}^{\text{carrier}},\overbrace{x_r^{(4)},y_r^{(4)},u_r^{(4)}}^{\text{ring}},\overbrace{x_s^{(4)},y_s^{(4)},u_s^{(4)}}^{\text{sun}},\overbrace{\zeta_{p1}^{(4)},\eta_{p1}^{(4)},u_{p1}^{(4)}}^{\text{planet-1}},\cdots,\overbrace{\zeta_{pn}^{(4)},\eta_{pn}^{(4)},u_{pn}^{(4)}}^{\text{planet-n}}}_{\text{fourth stage}}\end{array}\right) \tag{14}$$

$$\boldsymbol{T}=\left(\begin{array}{l}\underbrace{0,0,T_e}_{\text{rotor}},\underbrace{0,0,T_1,0,0,T_2,0,0,T_3}_{\text{first stage}},\underbrace{0,0,T_4,0,0,T_5,\cdots,0,0,T_8}_{\text{second stage}},\\ \underbrace{0,0,T_c^{(3)},0,0,T_r^{(3)},0,0,T_s^{(3)},0,\cdots 0}_{\text{third stage}},\underbrace{0,0,T_c^{(4)},0,0,T_r^{(4)},0,0,T_s^{(4)},0,\cdots 0}_{\text{fourth stage}}\end{array}\right)^T \tag{15}$$

$$\boldsymbol{F}(t)=\left(\begin{array}{l}\mathbf{0},\underbrace{\boldsymbol{F}_1,\boldsymbol{F}_2,\boldsymbol{F}_3}_{\text{first stage}},\underbrace{\boldsymbol{F}_4,\boldsymbol{F}_5,\cdots,\boldsymbol{F}_8}_{\text{second stage}},\underbrace{\mathbf{0},\sum\boldsymbol{F}_{rpn}^{(3)},\sum\boldsymbol{F}_{spn}^{(3)},\boldsymbol{F}_{p1}^{(3)},\cdots,\boldsymbol{F}_{pn}^{(3)}}_{\text{third stage}},\\ \underbrace{\mathbf{0},\sum\boldsymbol{F}_{rpn}^{(4)},\sum\boldsymbol{F}_{spn}^{(4)},\boldsymbol{F}_{p1}^{(4)},\cdots,\boldsymbol{F}_{pn}^{(4)}}_{\text{fouth stage}}\end{array}\right) \tag{16}$$

In which

$$\boldsymbol{F}_{rpn}=(k_{rpn}(t)e_{rpn}(t)+k_{rpn}(t)\dot{e}_{rpn}(t))\left[\sin\psi_{rn},-\cos\psi_{rn},1\right]^T \tag{17a}$$

$$\boldsymbol{F}_{spn}=(k_{spn}(t)e_{spn}(t)+k_{spn}(t)\dot{e}_{spn}(t))\left[\sin\psi_{sn},-\cos\psi_{sn},1\right]^T \tag{17b}$$

$$\begin{aligned}\boldsymbol{F}_{pn}=&(k_{spn}(t)e_{spn}(t)+k_{spn}(t)\dot{e}_{spn}(t))\left[\sin\alpha_s,\cos\alpha_s,1\right]^T+\\&+(k_{rpn}(t)e_{rpn}(t)+k_{rpn}(t)\dot{e}_{rpn}(t))\left[\sin\alpha_r,\cos\alpha_r,-1\right]^T\end{aligned} \tag{17c}$$

The STE excitation of the reduction gear in the parallel gear set can be expressed as:

$$\begin{aligned}\boldsymbol{F}_1(t)&=(k_{12}(t)e_{12}(t)+c_{12}(t)\dot{e}_{12}(t))\left[-\sin\psi_{12},-\cos\psi_{12},1\right]^T,\\ \boldsymbol{F}_3&=(k_{23}(t)e_{23}(t)+c_{23}(t)\dot{e}_{23}(t))\left[\sin\psi_{23},\cos\psi_{23},1\right]^T\end{aligned} \tag{18a}$$

$$\begin{aligned} \boldsymbol{F}_4(t) &= (k_{45}(t)e_{45}(t) + c_{45}(t)\dot{e}_{45}(t))\left[-\sin\psi_{45}, -\cos\psi_{45}, 1\right]^T, \\ \boldsymbol{F}_8 &= (k_{78}(t)e_{78}(t) + c_{78}(t)\dot{e}_{78}(t))\left[\sin\psi_{78}, \cos\psi_{78}, 1\right]^T \end{aligned} \tag{18b}$$

The STE excitation of the idler in the parallel gear set can be expressed as:

$$\begin{aligned} \boldsymbol{F}_i(t) = (k_{(i-1,i)}(t)e_{(i-1,i)}(t) + c_{(i-1,i)}(t)\dot{e}_{(i-1,i)}(t))\left[\sin\psi_{(i-1,i)}, \cos\psi_{(i-1,i)}, 1\right]^T - \\ (k_{(i,i+1)}(t)e_{(i,i+1)}(t) + c_{(i,i+1)}(t)\dot{e}_{(i,i+1)}(t))\left[\sin\psi_{(i,i+1)}, \cos\psi_{(i,i+1)}, -1\right]^T \end{aligned} \tag{19}$$

Where i denotes the number of the idler gears in the parallel gear set, $i = 2, 5, 6, 7$.

In these formulas, the TVMS for planetary gear set can be expanded in the form of Fourier series [29]:

$$k_{spn}(t) = \bar{k}_{spn} + \sum_{l=1}^{L} \hat{k}_{spl} \sin\left[l\omega_m(t + r_{sn}T_m) + \phi_{spl}\right] \tag{20a}$$

$$k_{rpn}(t) = \bar{k}_{rpn} + \sum_{l=1}^{L} \hat{k}_{rpl} \sin\left[l\left(\omega_m(t + r_{rn}T_m) + r_{sr}\right) + \phi_{rpl}\right] \tag{20b}$$

Where $\bar{k}_{spn}$ and $\bar{k}_{rpn}$ represent the mean value of gear mesh stiffness, $\hat{k}_{spl}$ and $\hat{k}_{rpl}$ represent the harmonic amplitudes, L represents the number of expanded harmonic, ω_m and T_m represent the mesh frequency and mesh cycle, respectively. γ_{sn} and γ_{rn} represent the mesh phase differences. ϕ_{spl} and ϕ_{rpl} represent the initial phase angles of the lth harmonic.

In these formulas, the STE for planetary gear set can also be expanded in the form of Fourier series [1]:

$$e_{spn}(t) = e_{sp0} + \sum_{l=1}^{L} \hat{e}_{spl} \sin\left[l\omega_m(t + r_{sn}T_m) + \phi_{spl}\right] \tag{21a}$$

$$e_{rpn}(t) = e_{rp0} + \sum_{l=1}^{L} \hat{e}_{rpl} \sin\left[l\left(\omega_m(t + r_{rn}T_m) + \gamma_{sr}\right) + \phi_{rpl}\right] \tag{21b}$$

Where e_{sp0} and e_{rp0} denote the mean values of STE, $\hat{e}_{spl}$ and $\hat{e}_{rpl}$ denote the harmonic amplitudes of STE.

3. Dynamic load excitations analysis in the system

The solutions of internal and external excitations are the basis for the system's dynamic response analysis in the SCSG. The external excitations mainly include the cutting torque of the drum and the electromagnetic torque of the motor in the coal-breaking process of the shearer. The motor torque has been obtained from formula (7), and the cutting torque of the drum is mainly discussed in this section. The internal excitations of the cutting section transmission system mainly include two types: stiffness excitation and error excitation.

3.1. External excitation of the system

The cutting heads used in longwall shearers are equipped with cutting picks. The cutting process of the picks requires generating sufficient force to overcome the resistance of coal and rock, which are dependent on the depth of cut, design parameters and cutting tool angles. Knowing the values of the forces that act on a single pick enables the reduction of these forces at the beginning of the shaft on which the cutting head is mounted. The forces reduced at the shaft of the cutting drum could be used as an external load excitation for the gearbox [30,31].

According to the coal-breaking mechanism, reference [32] proposed an average cutting force model during the process of breaking coal and rock with picks which are installed on a spiral drum. The picks' geometric parameters, the coal-breaking properties and the shearer traction speed are fully covered by the cutting resistance model. The cutting force Z_i of a single pick can be expressed as [32]:

$$Z_i = 10A_p \frac{0.35b_p + 0.3}{\left(b_p + Bh_i^{0.5}\right)\cos\beta} h_i \left(1.25h_i + b_p + 1.25\right) \frac{1.47B}{B+1.2} k_\varphi k_y k_{oT} \tag{22}$$

Where: A_p is the average cutting impedance of the coal seam (A_p = 280 ~ 560 N/mm), β is the installation angle of the pick, b_p is the working part width of the pick (b_p = 10 ~ 30 mm), B is the hardness coefficient of coal seam, h_i is the cutting thickness of coal seam, k_φ is the shape factor of front edge surface (k_φ = 0.85 ~ 0.9), k_y is the energy consumption coefficient of cutting angle (k_y = 0.9 ~ 1.34), k_{oT} is the mineral pressure coefficient (k_{oT} = 0.4 ~ 0.8).

The torque of the spiral drum could be obtained by the superposition of different pick forces. The force analysis of the spiral drum is shown in Fig. 5, in which α_i denotes the position angle of the i-th pick, h_{max} denotes the maximum cutting thickness of a single pick, d is the diameter of the drum.

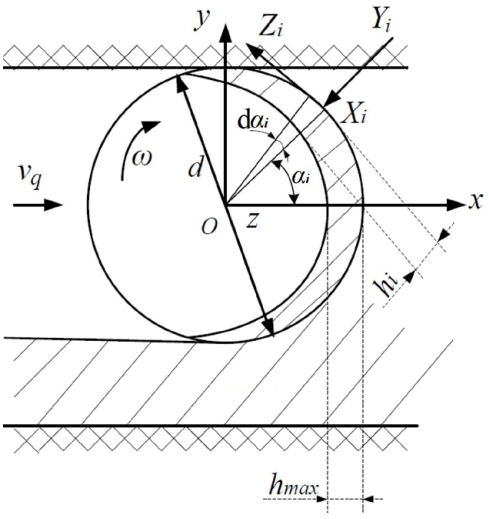

Fig. 5. Force analysis of spiral drum

The number of picks on the same line of the drum is defined as m, and then the cutting depth of the drum is $m \cdot h_{\max}$ for each circle. The total cutting depth s (unit: cm) of the shearer drum after t minutes satisfies the following relations:

$$s = v_q \cdot t \cdot 100 = h_{\max} \cdot m \cdot n \cdot t \tag{23}$$

Where: v_q represents the traction speed of the shearer, m/min; n denotes the rotation speed of the drum, r/min.

From the geometric relationship in Fig. 5, it can be concluded that:

$$h_i = h_{\max} \cos \alpha_i = \frac{100 v_q}{mn} \cos \alpha_i \tag{24}$$

The drum torque T_{out} can be expressed as:

$$T_{out} = \frac{1}{2} \sum_{i=1}^{m} Z_i d \tag{25}$$

3.2. Internal excitation of the system

Two types of internal excitations, time-varying mesh stiffness (TVMS) and static transmission error (STE) are mainly considered in the SCSG, which are solved in multi-stage parallel gear sets and two-stage planetary gear sets, respectively. The parameters for the first and second stages of parallel gear sets are illustrated in TABLE 1, and the design parameters for the third and fourth stages of planetary gear sets are listed in TABLE 2.

TABLE 1

Parameters of first and second stages parallel gear sets

Gear symbol	G_1	G_2	G_3	G_4	G_5	G_6	G_7	G_8
Number of teeth	28	39	40	27	33	33	33	40
Module /(mm)	8	8	8	10	10	10	10	10
Pressure angle (°)	20							
Mass/(kg)	13.5	27.1	28.4	25.1	35.1	35.1	35.1	52.4
Moment of inertia /(kg·m^2)	0.085	0.16	0.38	0.22	0.52	0.52	0.52	1.04
Bearing stiffness /(N/m)	10^9	10^9	10^9	2×10^9	2×10^9	2×10^9	2×10^9	2×10^9

TABLE 2

Parameters of third and fourth stages PGSs

	Number of teeth		**Module (mm)**		**Pressure angle (°)**		**Mass (kg)**		**Moment of inertia (kg·m^2)**		**Torsional stiffness (N/m)**		**Bearing stiffness (N/m)**	
Stage	3	4	3	4	3	4	3	4	3	4	3	4	3	4
Sun	18	18	7	11	20		5	10	0.04	0.06	0	0	10^9	2×10^9
Planet	32	24	7	11			12	29	0.07	0.23	0	0	10^9	2×10^9
Ring	82	66	7	11			33	108	1.36	7.11	10^9	2×10^9	10^9	2×10^9
Carrier	—	—	—	—	—	—	96	406	1.03	15.9	0	0	10^9	2×10^9

3.2.1. Dynamic excitation of multi-stage parallel gear sets

The TVMSs of multi-stage parallel gear sets are expanded by the Fourier series, and the results are illustrated in Fig. 6. Similarly, the STEs of parallel gear sets in the SCSG are shown in Fig. 7. According to the manufacturing and assembly accuracy class for the SCSG, the mean errors in the first-stage parallel gear sets are $\bar{e}_{12} = 6$ μm and $\bar{e}_{23} = 7$ μm, and the mean errors in the second-stage parallel gear sets are $\bar{e}_{45} = 7$ μm, $\bar{e}_{56} = 8$ μm, $\bar{e}_{67} = 8.5$ μm and $\bar{e}_{78} = 10$ μm.

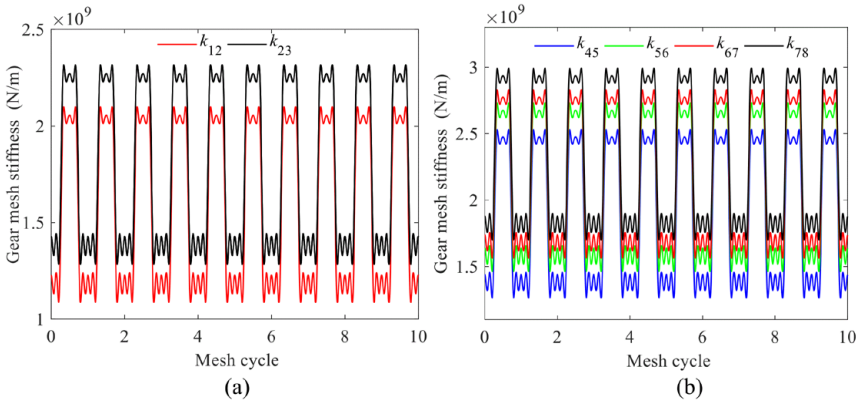

Fig. 6. The TVMS of multi-stage parallel gear sets, (a) the first-stage parallel gear sets, (b) the second-stage parallel gear sets

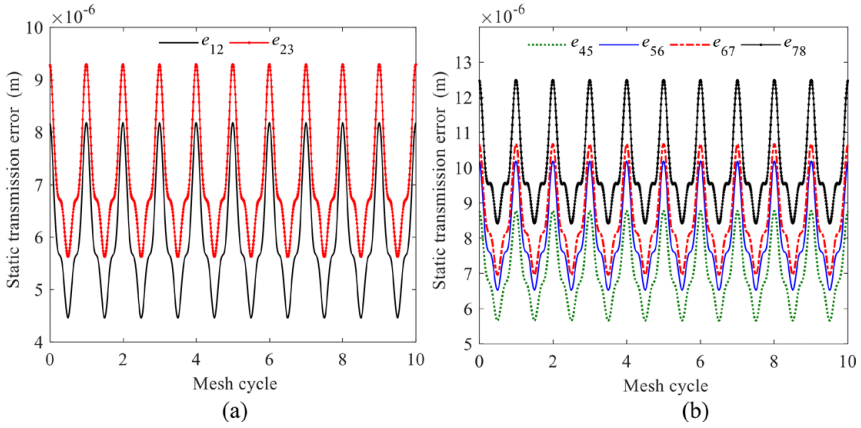

Fig. 7. The STE of multi-stage parallel gear sets, (a) the first-stage parallel gear sets, (b) the second-stage parallel gear sets

3.2.2. Dynamic excitation of two-stage PGSs

The relevant parameters of two-stage PGSs are shown in TABLE 1, and the number of planet gears is $N^{(3)} = N^{(4)} = 4$. Since the planets are uniformly distributed around the sun, the initial

position angles of the planets are $\psi_1 = 0$, $\psi_2 = \pi/2$, $\psi_3 = \pi$, $\psi_4 = 3\pi/2$, respectively. γ_{si} is defined as the phase difference between the ith planet-sun mesh pair relative to the first planet-sun mesh pair, taken as $\gamma_{s1} = 0$, and γ_{ri} is defined as the phase difference between the ith planet-ring mesh pair relative to the first planet-ring mesh pair.

The mesh phase condition is determined by Reference [29], so the mesh phase difference between planet-sun and planet-ring in the third-stage PGS can be expressed as:

$$\begin{Bmatrix} \gamma_{s1}^{(3)} \\ \gamma_{s2}^{(3)} \\ \gamma_{s3}^{(3)} \\ \gamma_{s4}^{(3)} \end{Bmatrix} = \frac{18}{2\pi} \begin{Bmatrix} 0 \\ \frac{\pi}{2} \\ \pi \\ \frac{3\pi}{2} \end{Bmatrix} = \begin{Bmatrix} 0 \\ \frac{9}{2} \\ 9 \\ \frac{27}{2} \end{Bmatrix} \rightarrow \begin{Bmatrix} 0 \\ \frac{1}{2} \\ 0 \\ \frac{1}{2} \end{Bmatrix} \tag{26a}$$

$$\begin{Bmatrix} \gamma_{r1}^{(3)} \\ \gamma_{r2}^{(3)} \\ \gamma_{r3}^{(3)} \\ \gamma_{r4}^{(3)} \end{Bmatrix} = -\frac{82}{2\pi} \begin{Bmatrix} 0 \\ \frac{\pi}{2} \\ \pi \\ \frac{3\pi}{2} \end{Bmatrix} = -\begin{Bmatrix} 0 \\ \frac{41}{2} \\ 41 \\ \frac{123}{2} \end{Bmatrix} \rightarrow \begin{Bmatrix} 0 \\ -\frac{1}{2} \\ 0 \\ -\frac{1}{2} \end{Bmatrix} \tag{26b}$$

The mesh phase condition for the fourth-stage PGS can be expressed as

$$\begin{Bmatrix} \gamma_{s1}^{(4)} \\ \gamma_{s2}^{(4)} \\ \gamma_{s3}^{(4)} \\ \gamma_{s4}^{(4)} \end{Bmatrix} = \frac{18}{2\pi} \begin{Bmatrix} 0 \\ \frac{\pi}{2} \\ \pi \\ \frac{3\pi}{2} \end{Bmatrix} = \begin{Bmatrix} 0 \\ \frac{9}{2} \\ 9 \\ \frac{27}{2} \end{Bmatrix} \rightarrow \begin{Bmatrix} 0 \\ \frac{1}{2} \\ 0 \\ \frac{1}{2} \end{Bmatrix} \tag{27a}$$

$$\begin{Bmatrix} \gamma_{r1}^{(4)} \\ \gamma_{r2}^{(4)} \\ \gamma_{r3}^{(4)} \\ \gamma_{r4}^{(4)} \end{Bmatrix} = -\frac{66}{2\pi} \begin{Bmatrix} 0 \\ \frac{\pi}{2} \\ \pi \\ \frac{3\pi}{2} \end{Bmatrix} = -\begin{Bmatrix} 0 \\ \frac{33}{2} \\ 33 \\ \frac{99}{2} \end{Bmatrix} \rightarrow \begin{Bmatrix} 0 \\ -\frac{1}{2} \\ 0 \\ -\frac{1}{2} \end{Bmatrix} \tag{27b}$$

The TVMS for the third-stage PGS which is calculated based on the design parameters, phase values is illustrated in Fig. 8, and the TVMS for the fourth-stage PGS is illustrated in Fig. 9. If the mesh phase between planet-1 and sun is 0, then the mesh phases between planet-2, planet-3, planet-4 and sun lag planet-1 and sun by 1/2, 0, and 1/2 mesh cycles, respectively. The mesh phases between planet-2, planet-3, planet-4 and ring are 1/2, 0, and 1/2 mesh cycles ahead of planet-1 and sun.

Similarly, the STE for two-stage PGSs is expanded in the Fourier series based on formula (21). On the premise of ensuring solution accuracy, the STE is only expanded to the third item by

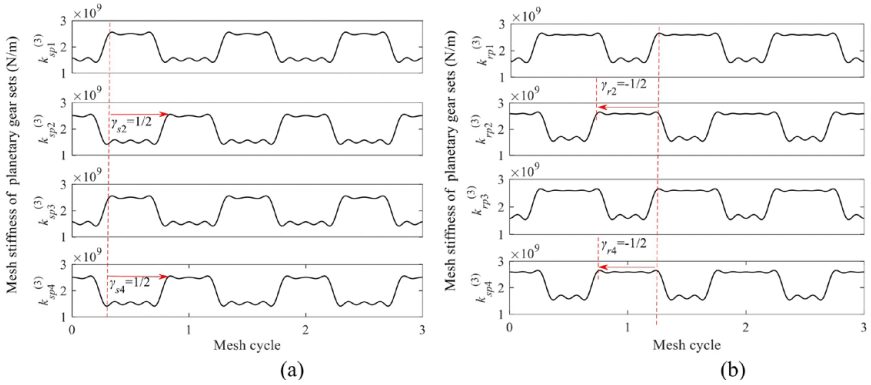

Fig. 8. The TVMS of the third-stage PGS, (a) sequential phase mesh of planet-sun, (b) sequential phase mesh of planet-ring

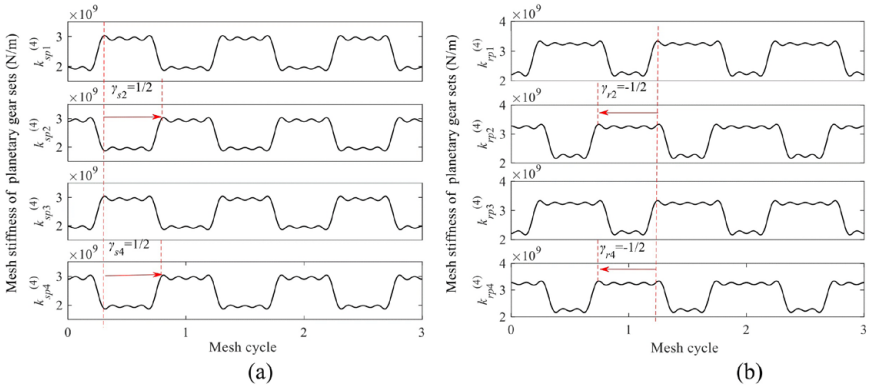

Fig. 9. The TVMS of the fourth-stage PGS, (a) sequential phase mesh of planet-sun, (b) sequential phase mesh of planet-ring

considering the complexity of solving the system's dynamic response. The phase conditions for STE in the PGSs are the same as in TVMS. Therefore, only the STE for external $s-p_1$ gear pair and internal $r-p_1$ gear pair are shown in Fig. 10, while the STE for external and internal gear pairs of planet-2, planet-3, and planet-4 are only different in phase. According to the manufacturing and assembly accuracy class for the SCSG, the mean errors in the third-stage PGS are taken as $e_{sp0}^{(2)} = 7$ μm and $e_{rp0}^{(2)} = 8$ μm, and the mean errors in the fourth-stage PGS are taken as $e_{sp0}^{(1)} = 10$ μm and $e_{rp0}^{(1)} = 12$ μm.

4. Numerical simulation

The Numerical integration function of MATLAB is used to acquire the dynamic time response of the mechanical and electrical system in the SCSG, that is, the variable step size Runge-Kutta method is adopted to solve the kinematic differential formula (13) of the coupled system. The

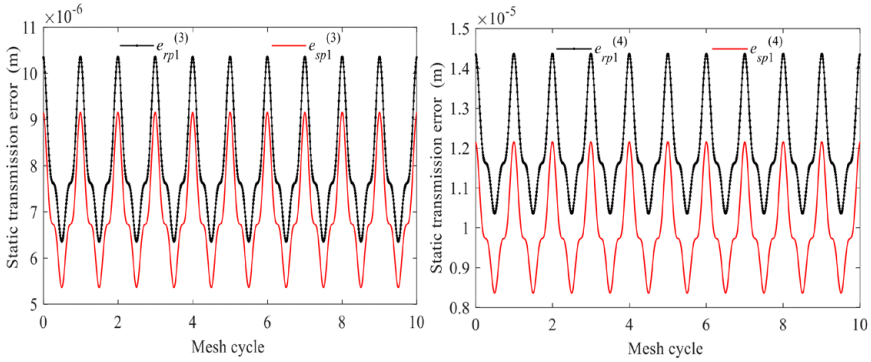

Fig. 10. The STE of two-stage PGSs, (a) the third stage PGS, (b) the fourth stage PGS

design parameters of the SCSG have been listed in TABLE 1 and TABLE 2, and the system parameters of the motor are listed in TABLE 3. The output speed of the drum is 30 r/min, and the traction speed of the shearer is 3 m/min.

TABLE 3

System parameters of asynchronous motor

Nameplate parameters		**Circuit parameters**	
Rated power supply frequency	50 Hz	R_{st}	0.7754 Ω
Rated supply voltage	3300 V	R_{ro}	0.7979 Ω
Rated power	500 kW	L_m	0.3351 H
Rated speed	1470 rpm	L_{st}	0.3399 H
Rated current	109 A	L_{ro}	0.3399 H

According to the working conditions of the shearer, the mesh frequencies of the transmission system at all stages and the power supply frequency can be found in TABLE 4, f_{n1} and f_{n2} denote mesh frequencies of the first and second stages parallel gear sets, f_{c3} and f_{c4} denote rotation frequencies of the third and fourth stages planetary carriers, and f_e represents the power supply frequency.

TABLE 4

Mesh frequency and power supply frequency for electromechanical transmission system (unit: Hz)

Title	**Mesh frequency and rotation frequency**						**Supply frequency**
Symbol	f_{n1}	f_{n2}	f_{m3}	f_{m4}	f_{c3}	f_{c4}	f_e
Value	686	465.8	180	30	2.33	0.5	50

The mesh frequencies f_{m3} and f_{m4} for the third and fourth stages of planetary gear sets can be expressed as:

$$f_{m3} = \left(n_{s3}/60\right) \times z_{s3} \times z_{r3} / \left(z_{r3} + z_{s3}\right) \tag{28a}$$

$$f_{m4} = (n_{s4}/60) \times z_{s4} \times z_{r4} / (z_{r4} + z_{s4}) \tag{28b}$$

Where: n_{s3} and n_{s4} respectively indicate the speeds of the third and fourth stage suns, in unit r/min. z_{s3}, z_{s4} and z_{r3}, z_{r4} represent the teeth numbers for the suns and planets, respectively.

4.1. Dynamic response of the system

Two-stage planetary gear sets of the SCSG undertake the main deceleration task, and their internal dynamic responses are more complex. The vibration characteristics of two-stage planetary gear sets are mainly displayed. Fig. 11 shows the relationship between vibration displacement and time in the x and y directions for the third-stage planetary central members. From Fig. 11, it can be seen that the vibration displacement of each central member presents a periodic variation pattern, and its vibration period is 0.428 s, which is exactly consistent with the rotation period of the third stage carrier. The vibration amplitude of sun gear is more evident than other central components, and its peak in the x direction is 134% larger than that in the y direction. Therefore, more attention should be paid to the vibration in the x direction for the PGSs.

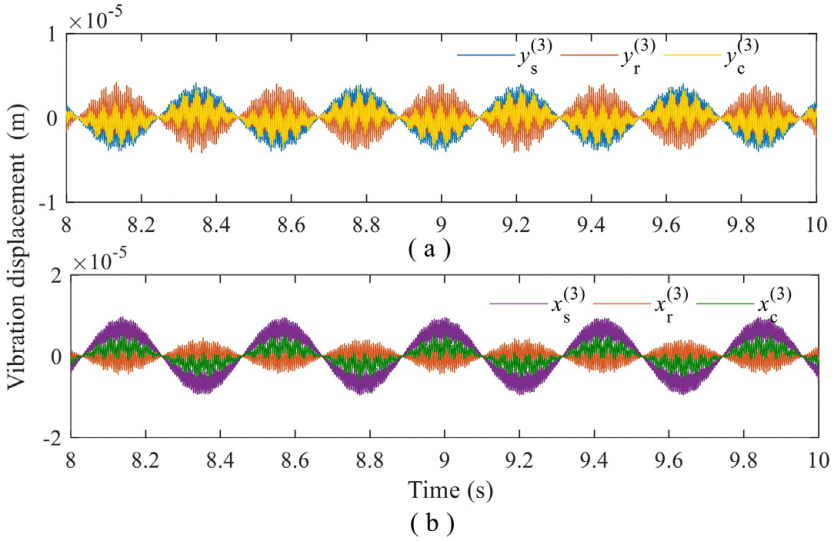

Fig. 11. Vibration displacement time history of sun, ring and carrier for the third stage PGSs: (a) vibration displacement in the y direction, (b) vibration displacement in the x direction

The relationship between vibration displacement and time can be observed from Fig. 12 in the x and y directions for the fourth-stage PGSs. The vibration amplitude of the ring in the fourth-stage PGS is more obvious than other members. However, the vibration peak of the ring differs by only 13.6% in the x and y directions, indicating that the fluctuation amplitude of the fourth-stage PGS along all directions is more balanced than that of the third-stage PGS. This is mainly related to the coupling connection between the fourth-stage carrier and spiral drum, which undertakes a heavy load.

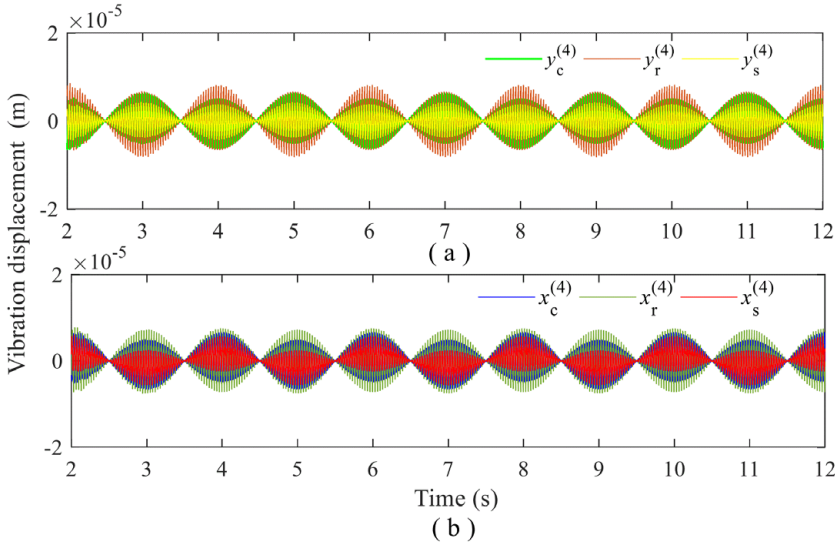

Fig. 12. Vibration displacement and time relation of center components for the fourth-stage PGS in the x and y directions: (a) vibration displacement in the y direction, (b) vibration displacement in the x direction

4.2. Dynamic meshing force analysis

The fourth-stage carrier of the SCSG is coupled with a spiral drum, and the dynamic load-sharing behaviour of two-stage PGSs directly determines the service life of the SCSG. The time history curves of the dynamic meshing force between the planet and ring in two-stage PGSs are presented in Fig. 13. It can be seen from Fig. 13 that dynamic meshing forces exhibit periodic fluctuations in the PGSs, and the vibration period is the rotation period of the carrier. The dynamic force level of the fourth-stage PGS is higher, with a peak value of about 2.74 times that of the third stage. The load sharing of different gear pairs is not uniform in a planetary gear set.

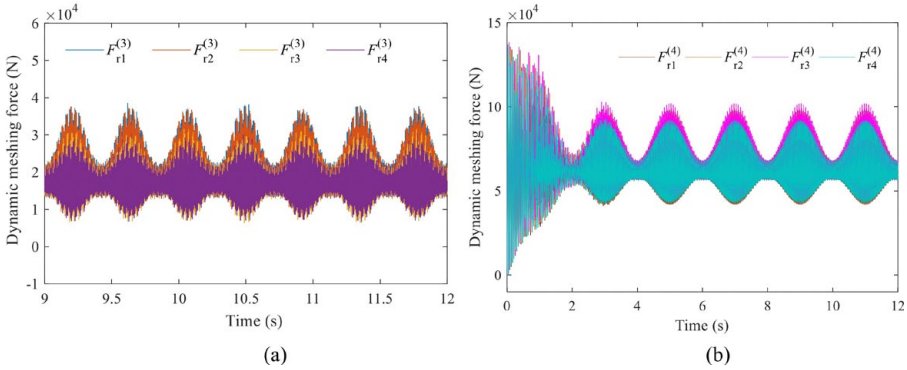

Fig. 13. Dynamic meshing force for planet-ring in two-stage PGSs: (a) meshing force $F_{rn}^{(3)}$ (n = 1, 2, …, N) for third-stage PGS, (b) meshing force $F_{rn}^{(4)}$ (n = 1, 2, …, N) for fourth-stage PGS

To further explore the sources and categories of dynamic excitation in the SCSG, frequency analysis is conducted for dynamic meshing force in two-stage PGSs. Fig. 14 demonstrates the frequency response of meshing force $Fr_1^{(4)}$ in the fourth-stage PGS.

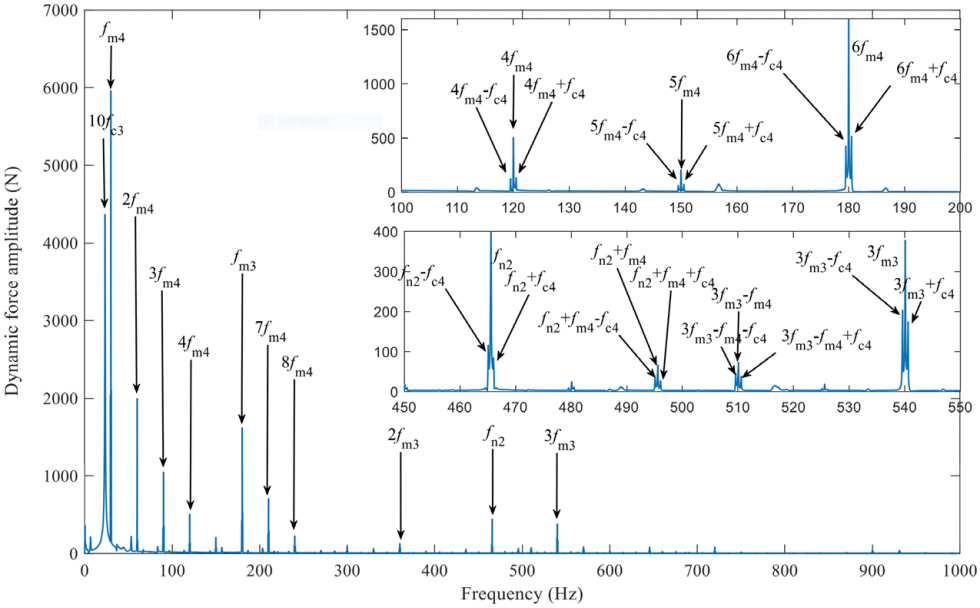

Fig. 14. Frequency response of meshing force $Fr_1^{(4)}$ in the fourth-stage PGS

It can be seen from Fig. 14 that signal energy fluctuation of dynamic meshing force for planetary gear is mainly caused by the excitation related to the meshing frequencies. For example, when the excitation frequency is 30 Hz, it excites the harmonic energy peak of dynamic force, and 30 Hz exactly matches the meshing frequency f_{m4} for the fourth-stage PGS. Similarly, when the excitation frequencies are 60 Hz ($2f_{m4}$), 90 Hz ($3f_{m4}$), and 180 Hz (f_{m3}), harmonic energies of dynamic forces are also excited to a large extent. This indicates that TVMS and STE of spur gears are the main excitation sources for vibration signal energy.

It can be concluded that excitation frequencies of dynamic forces in fourth-stage PGS mainly include meshing frequency f_{m4} and its harmonic components, as well as coupling frequencies of all stages. At the same time, the frequency modulation phenomenon is formed with meshing frequency f_{m4} as carrier frequency and rotation frequency f_{c4} as the sideband. The modulation frequencies comprise $if_{m4} \pm f_{c4}$ (i = 3, 4, 5), $jf_{m3} \pm f_{c4}$ (j = 1, 2, 3), $f_{n2} + f_{m4} \pm f_{c4}$, etc.

Excitation frequencies of the third stage PGS are more abundant than that of the fourth stage, as shown in Fig. 15. The inter-stage coupling effect is more obvious for third-stage PGS, and the signal energies excited by meshing frequencies f_{m3}, f_{m4} and their harmonics are more prominent. From the local focus of the spectrum, there is a frequency modulation phenomenon in the third-stage PGS, which takes each stage meshing frequency as carrier frequency and rotation frequency f_{c3} as the sideband. This also illustrates the multi-source and coupling characteristics of the excitation sources for the signal energies in multi-stage PGSs.

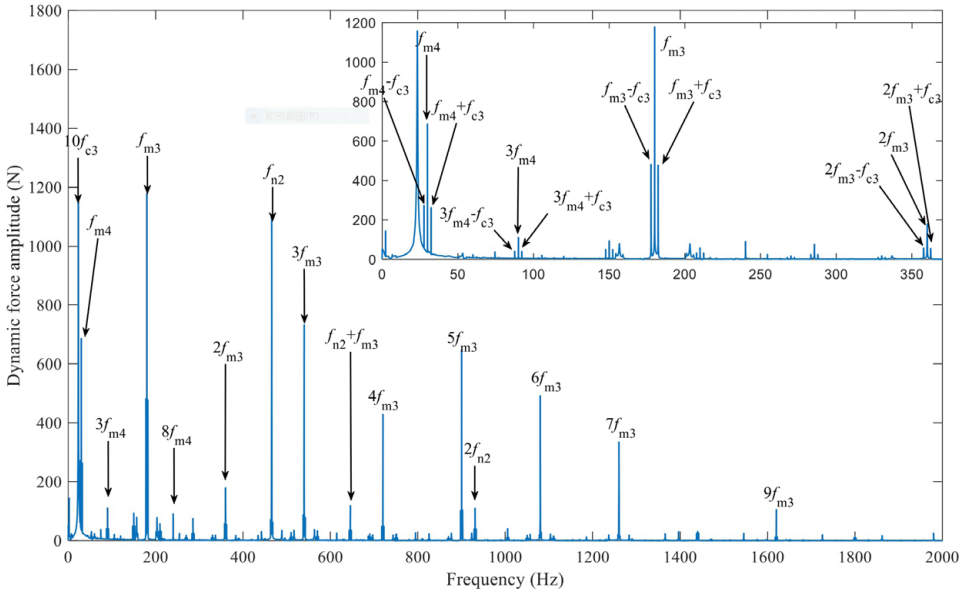

Fig. 15. Frequency response of meshing force $Fr_1^{(3)}$ in the third-stage PGS

At the same time, the uniformity of load distribution has a significant impact on the vibration stability and carrying capacity for planetary gear systems. Load sharing coefficient (LSC) is generally used to weigh the load distribution status between different meshing pairs in planetary gear transmission systems, load sharing coefficient of the n-th planetary gear can be defined as [33]:

$$\begin{cases} h_{spni} = \dfrac{N(F_{spni})_{\max}}{\sum_{n=1}^{N}(F_{spni})_{\max}} \\ h_{rpni} = \dfrac{N(F_{rpni})_{\max}}{\sum_{n=1}^{N}(F_{rpni})_{\max}} \end{cases} \tag{29}$$

Where $(F_{spni})_{\max}$ and $(F_{rpni})_{\max}$ represent the maximum values of external and internal meshing forces for the n-th (n = 1, 2,..., N) planet in the i-th meshing cycle. h_{spni} and h_{rpni} are the LSC of the n-th planet in the i-th meshing cycle.

H_{sp} and H_{rp} are the LSCs of PGS for external and internal meshing pairs, respectively, and can be defined as [33]:

$$\begin{cases} H_{sp} = (h_{spni})_{\max} \\ H_{rp} = (h_{rpni})_{\max} \end{cases} \tag{30}$$

Fig. 16 shows the LSC of gear pairs between different planets and rings in fourth-stage PGS. Planets with an initial phase difference of 180° have almost the same load-sharing characteristics,

while planets with an initial phase difference of 90° have distinct load distribution to some extent. Static transmission error excitation equation is derived for multi-stage gear sets in this paper, the relationship between LSC and drum torque is established under different error excitation conditions, as shown in Fig. 17. It can be seen from Fig. 17 that H_{rp} decreases with the increase of load torque, indicating that load-sharing performance is improved when the load increases in the PGS. In addition, the STE will aggravate the vibration intensity between different planetary gear pairs, which will reduce the load sharing performance in the PGS.

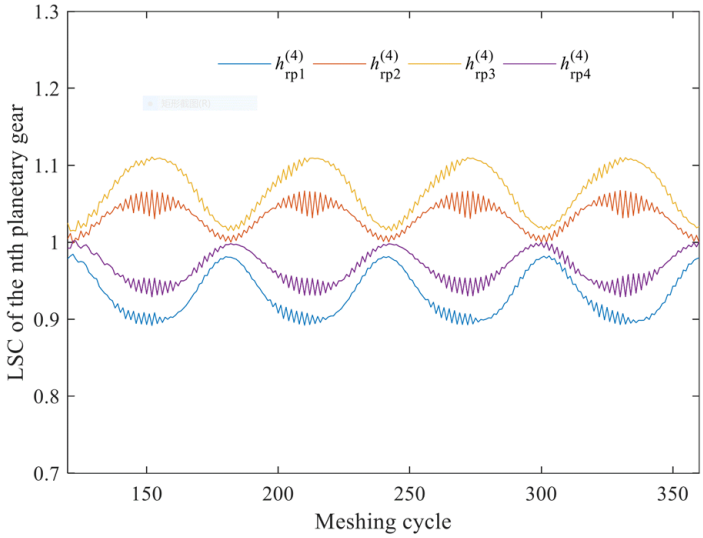

Fig. 16. LSC of gear pairs between different planets and rings in fourth-stage PGS

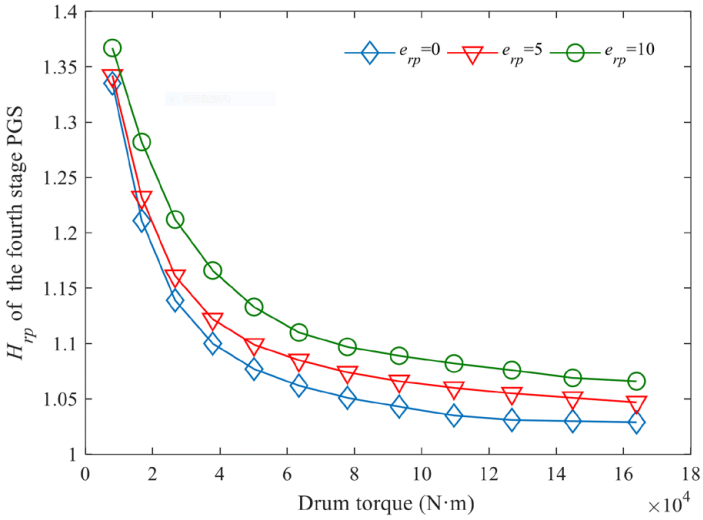

Fig. 17. Relationship between LSC and drum torque under different STE (the unit of e_{rp} is μm)

Traction speed (v_q) is the shearer's horizontal movement speed parallel to the working coal wall. Traction speed is the important indicator that directly determines the mining efficiency of the shearer. If the traction speed is increased, the shearer needs to cut more coals and rocks at the same time, that is, the shearer cutting section will bear greater forces, which is also verified in formulas (22)-(24) within the force model of the shearer drum. To further reveal the influence mechanism between the mining rate and dynamic property of the SCSG, the distribution rule of LSC is presented in the fourth-stage PGS at different traction speeds, as shown in Fig. 18. It could be found that traction speed has a significant impact on the LSC of planetary gears. H_{rp} and H_{sp} both decrease with the increase in traction speed. An increasing torque would further enlarge the relative displacement of gear pairs, thereby reducing the proportion of transmission errors in the relative displacement. Consequently, the load-sharing performance of the planetary system is improved. This indicates that load-sharing performance can be effectively guaranteed in the process of increasing the coal mining rate.

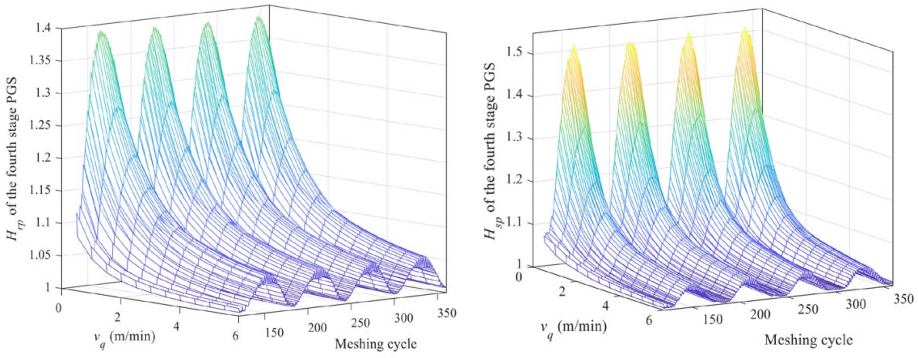

(a) (b)

Fig. 18. Distribution rule of LSC in the fourth-stage PGS at different traction speeds, (a) H_{rp} between ring and planet, (b) H_{sp} between sun and planet

5. Experimental verification and coupling characteristic analysis of electromechanical model

In this paper, a dynamic mechatronics model is proposed through coupling the shearer motor and multistage gear transmission system. The fluctuating current signals of the motor are tested under different mining conditions to verify the accuracy of the simulation model. Furthermore, the interaction mechanism is revealed between mechanical and electrical systems for the shearer cutting section.

5.1. Experimental verification of mechatronics integration model

The dynamic experiment for the shearer has been completed at the National Energy Mining Equipment Experimental Center in Zhangjiakou City, China. The experimental system of fully mechanized mining equipment includes a double-drum shearer (Model MG500/1180 with

a cutting power of 500 kW), a hydraulic support (Model YZ9000/15/28D), and a scraper conveyor (Model SGZ1000/1050). The experimental system of fully mechanized mining equipment is shown in Fig. 19. The test conditions of the shearer are as follows: the cutting depth of the drum is 300 mm, and the rotation speed of the drum is 30 r/min. The traction speed v_q is accelerated from 0 to 5 m/min and current signals are acquired in real time.

Fig. 19. Experimental system of fully mechanized mining equipment

The comparison results of motor current effective values under experimental and simulation conditions in the accelerated cutting process of shearer are shown in Fig. 20. In the process of coal breaking, drum torque is affected by the hardness of coal rock, the pressure of coal wall and the randomness of coal falling particles, so the scatters of experimental data for current have a certain amount of fluctuation. It can be seen from Fig. 20 that the root mean square (RMS)

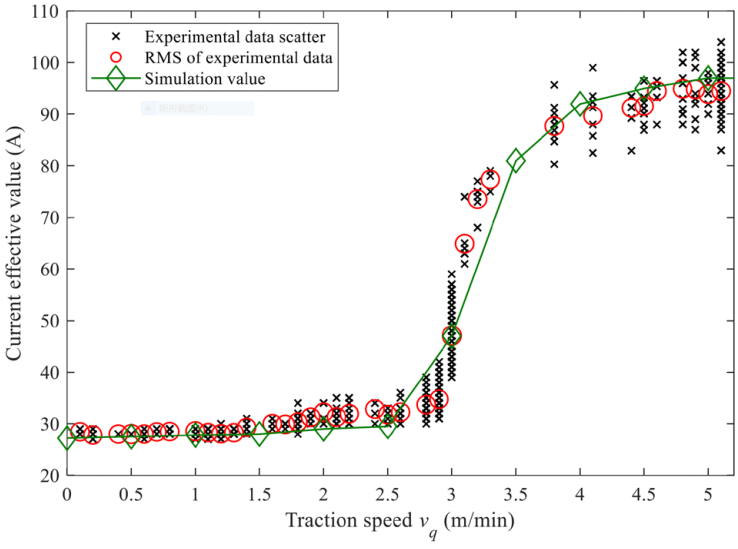

Fig. 20. Comparison results of motor current effective values under experimental and simulation conditions

values of experimental data have a good consistency with the simulation analysis results, thus verifying the accuracy of the mechatronics model proposed in this paper.

5.2. The interaction of mechanical and electrical systems

The functional relationship between traction speed v_q and drum torque Tout can be found in equations (22)-(25), drum torque will increase synchronously with traction speed. To study the effect of traction speed v_q on the dynamic characteristics of the electromechanical coupling system, dynamic responses are solved at different traction speeds.

Dynamic responses are solved by traction speed gradually changing from 0.5 m/min to 3 m/min. Fig. 21 illustrates the time response for the stator current at different traction speeds, It can be seen that the stator current increases with the traction speed, indicating that when the shearer accelerates mining, the motor withstands larger mechanical torque, so it needs to output stronger current to balance this change. When internal excitation caused by STE is incorporated into the dynamic model, the stator current in the simulation results is significantly stronger than that errorless case in the model. Errors caused by manufacturing and assembly would change the relative displacement of the gear meshing pair, thereby increasing the dynamic meshing force for the meshing pair. Therefore, the gear error would make the transmission system produce a greater dynamic load. When the system load increases, the motor needs to output a larger current to maintain power matching. Therefore, the electromechanical simulation model incorporating the STE has better guidance for correctly evaluating motor current and preventing system overload operation.

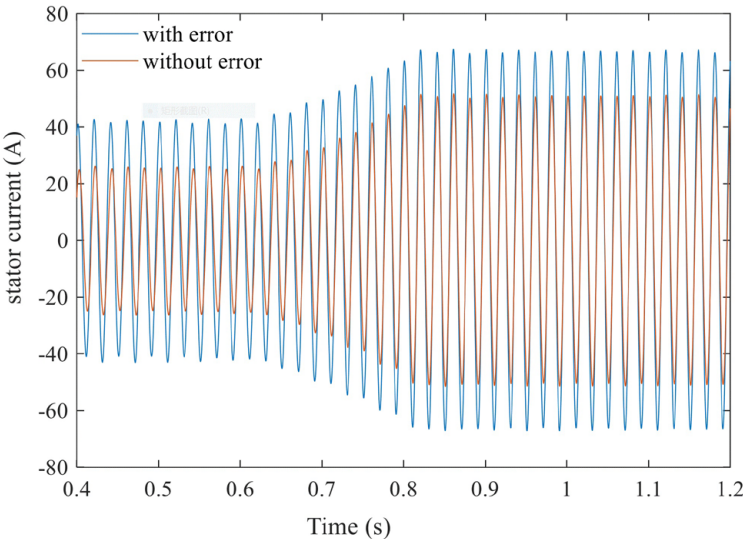

Fig. 21. Time response of stator current under different traction speeds

Fig. 22 shows the time response of the ABC three-phase stator current when the traction speed v_q is 3 m/min. Fig. 23 illustrates the spectrum of stator current signal after the Fast Fourier Transform (FFT). Compared with the supply frequency f_e, the mechanical vibration signal

belongs to the small amplitude frequency in the current spectrum, and it is difficult to observe the mechanical vibration signal in the current spectrum by using ordinary linear coordinates. Therefore, to highlight the role of mechanical system signals, the current spectrum is displayed in the logarithmic coordinate system.

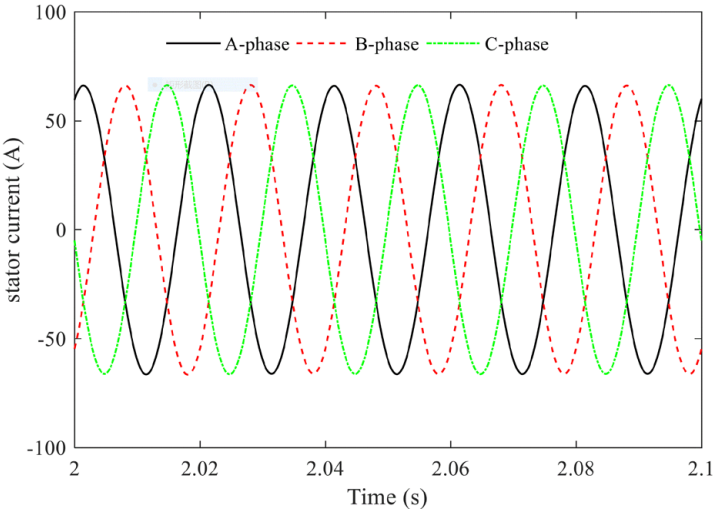

Fig. 22. Time response of three-phase stator current when traction speed v_q = 3 m/min

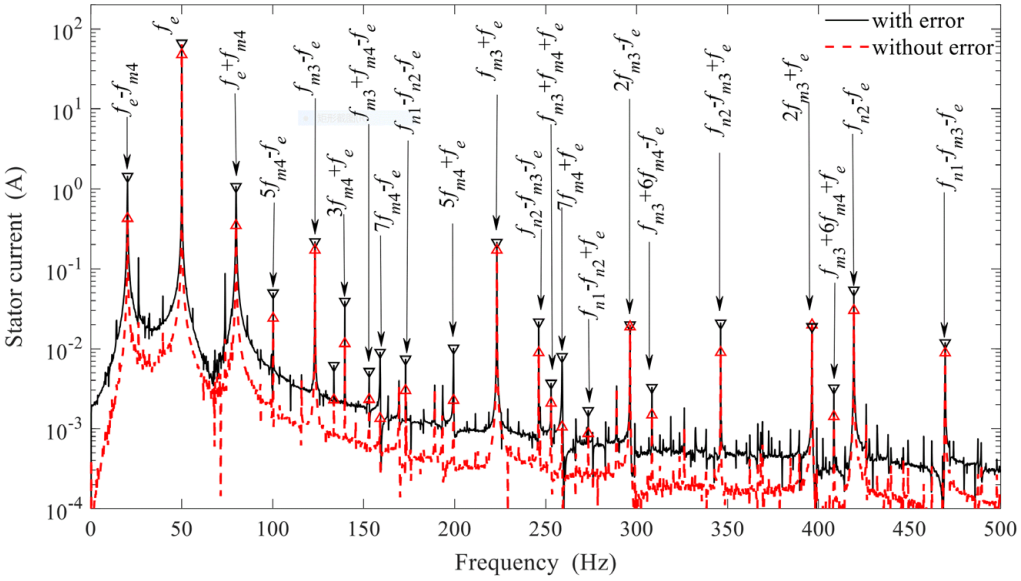

Fig. 23. The spectrum of three-phase stator current when traction speed v_q = 3 m/min

In Fig. 23, the spectrum peak of the stator current appears at supply frequency f_e, and the frequency modulation (FM) phenomenon occurs with supply frequency as the carrier and mechanical vibration frequency as the sideband.

The sideband components include: Mesh frequency sidebands ($|f_{n1} \pm f_e|$) for the first-stage parallel gear sets, mesh frequency sidebands ($|f_{n2} \pm f_e|$) for the second-stage parallel gear sets, mesh frequency sidebands ($|jf_{m3} \pm f_e|, j = 1, 2$) for the third-stage PGS, mesh frequency sidebands ($|if_{m4} \pm f_e|, i = 1, 3, 5, 7$) for the fourth-stage PGS, related terms of inter-stage coupling frequencies ($|(f_{m3} + f_{m4}) \pm f_e|, |(f_{n1} - f_{n2}) - f_e|, |(f_{n2} - f_{m3}) + f_e|, f_{n1} - f_{m3} - f_e$), etc.

Due to space limitations, Fig. 23 only presents frequency components ranging from 0 to 500 Hz. It can be found from the current spectrum that there is a lot of vibration information related to the mechanical system in asynchronous motor current signal, which indicates that the motor current signal can be used to monitor the complex vibration in the SCSG.

6. Conclusion

Taking the SCSG as the research object, detailed studies have been carried out on system dynamic modelling, internal dynamic excitation analysis, electromechanical coupling dynamic characteristics analysis and mechatronics experiment verification. The main research contents and conclusions include:

(1) The translation-torsional coupling dynamic model is developed for two-stage planetary gear sets and multi-stage parallel gear sets. Through the connection relationship between the motor and transmission system, a coupling mechatronic model is established between the multi-stage gear system and the motor. The matrix assembly method with inter-stage coupling is efficient for the simulation of large and complex mechanical models.

(2) The frequency response and order analysis of dynamic meshing force for two stage PGSs show that there exists a meshing frequency modulation phenomenon in the PGS, which takes meshing frequencies f_{m3} and f_{m4} as carrier frequency and rotation frequencies f_{c3} and f_{c4} as the sideband. The LSC of planetary gear sets gradually approaches 1 with the drum torque increasing, which indicates that load-sharing performance can be effectively guaranteed in the process of increasing the coal mining rate.

(3) Current signals of the motor are tested at different mining rates and have a good agreement with the simulation value, thus verifying the accuracy of the simulation model. Subsequently, motor current signature analysis is conducted by the mechatronics coupling model. The peak of the current spectrum appears at supply frequency f_e, and the frequency modulation (FM) phenomenon occurs with supply frequency as the carrier and mechanical vibration frequencies as the sidebands. These results indicate that stator currents can be used to monitor the vibration signal of the gearbox.

Acknowledgment

We would like to express our appreciation to National Natural Science Foundation of China (Grant Nos. 52302521, U23B2098, 52372365 and 52402484) and Young Innovative Talents Project of Guangdong Education Department of China (Grant No. 2022KQNCX099) for supporting this research. We would also like to thank the Zhaoqing Science and Technology Innovation Project (Grant No. 2022040305005) for supporting this research.

Declaration of Interest Statement

On behalf of all authors, the corresponding author states that there is no conflict of interest.

References

[1] A. Kahraman, Load Sharing Characteristics of Planetary Transmissions. Mech. Mach. Theory **29** (8), 1151-1165 (1994). DOI: https://doi.org/10.1016/0094-114X(94)90006-X

[2] A. Kahraman, Planetary Gear Train Dynamics. J. Mech. Design **116** (3), 713-720 (1994). DOI: https://doi.org/10.1115/1.2919441

[3] M. Inalpolat, A. Kahraman, A Theoretical and Experimental Investigation of Modulation Sidebands of Planetary Gear Sets. J. Sound Vib. **323**, 677-696 (2009). DOI: https://doi.org/10.1016/j.jsv.2009.01.004

[4] M. Inalpolat, A. Kahraman, A Dynamic Model to Predict Modulation Sidebands of a Planetary Gear Set Having Manufacturing Errors. J. Sound Vib. **329** (4), 371-393 (2010). DOI: https://doi.org/10.1016/j.jsv.2009.09.022

[5] C.J. Bahk, R.G. Parker, Analytical Solution for the Nonlinear Dynamics of Planetary Gears. J. Comput. Nonlin. Dyn. **6** (2), 021007 (2011). DOI: https://doi.org/10.1115/1.4002392

[6] D. Sheng, R. Zhu, G. Jin, F. LU, H. Bao, Dynamic Load Sharing Behavior of Transverse-Torsional Coupled Planetary Gear Train with Multiple Clearances. J. Cent. South Univ. **22** (7), 2521-2532 (2015). DOI: https://doi.org/10.1007/s11771-015-2781-6

[7] Z. Cao, Y. Shao, M. Rao, W. Yu, Effects of the Gear Eccentricities on the Dynamic Performance of a Planetary Gear Set. Nonlinear Dyn. **91** (1), 1-15 (2018). DOI: https://doi.org/10.1007/s11071-017-3738-0

[8] J.I. Pedrero, M. Pleguezuelos, M.B. Sánchez, Influence of Meshing Stiffness on Load Distribution Between Planets of Planetary Gear Drives. Mech. Mach. Theory **170**, 104718 (2022). DOI: https://doi.org/10.1016/j.mechmachtheory.2021.104718

[9] W. Sun, X. Li, J. Wei, A. Zhang, X. Hu, A Study on Load-Sharing Structure of Multi-stage Planetary Transmission System. J. Mech. Sci. Technol. **29** (4), 1501-1511(2015). DOI: https://doi.org/10.1007/s12206-015-0323-7

[10] L. Zhang, Y. Wang, K. Wu, R. Sheng, Three-Dimensional Modeling and Structured Vibration Modes of Two-Stage Helical Planetary Gears Used in Cranes. Shock Vib. **2017**, 1-18 (2017). DOI: https://doi.org/10.1155/2017/9864959

[11] H. Zhai, C. Zhu, C. Song, H. Liu, H. Bai, Influences of Carrier Assembly Errors on the Dynamic Characteristics for Wind Turbine Gearbox. Mech. Mach. Theory **103**, 138-147 (2016). DOI: https://doi.org/10.1016/j.mechmachtheory.2016.04.015

[12] S. Mo, S. Ma, G. Jin, Y. Zhang, C. Lv, H. Houjoh, Research on Multiple-Split Load Sharing Characteristics of 2-Stage External Meshing Star Gear System in Consideration of Displacement Compatibility. Math. Probl. Eng. **2017** (1), 1037479 (2017). DOI: https://doi.org/10.1155/2017/1037479

[13] A. Hammami, A. Fernandez Del Rincon, F. Chaari, F. Viadero Rueda, M. Haddar, Dynamic Behaviour of Back to Back Planetary Gear in Run up and Run down Transient Regimes. J. Mech. **31** (4), 481-491 (2015). DOI: https://doi.org/10.1017/jmech.2014.95

[14] A. Hammami, A. Fernandez Del Rincon, F. Chaari, M.I. Santamaria, F.V. Rueda, M. Haddar, Effects of Variable Loading Conditions on the Dynamic Behavior of Planetary Gear with Power Recirculation. Measurement **94**, 306-315 (2016). DOI: https://doi.org/10.1016/j.measurement.2016.07.083

[15] A. Mbarek, A. Fernandez Del Rincon, A. Hammami, M. Iglesias, F. Chaari, F. Viadero, M. Haddar, Comparison of Experimental and Operational Modal Analysis on a Back to Back Planetary Gear. Mech. Mach. Theory **124**, 226-247 (2018). DOI: https://doi.org/10.1016/j.mechmachtheory.2018.03.005

[16] A. Mężyk, Minimization of Transient Forces in Anelectro-Mechanical System. Struct. Optimization **8**, 251-256 (1994). DOI: https://doi.org/10.1007/BF01742711

[17] A. Mężyk, Modelling and Optimization of Transmission Systems with an Asynchronous Motor. J. Thero. Appl. Mech. **41** (01), 169-197 (2003).

[18] E. Świtoński, A. Mężyk, Selection of Optimum Dynamic Features for Mechatronic Drive Systems. Automat. Constr. **17** (3), 251-256 (2008). DOI: https://doi.org/10.1016/j.autcon.2007.05.001

[19] A. Mężyk, W. Klein, M. Fice, M. Pawlak, K. Basiura, Mechatronic Model of Continuous Miner CuttingDrum Driveline. Mechatronics **37**, 12-20 (2016). DOI: https://doi.org/10.1016/j.mechatronics.2015.11.004

[20] W. Bai, D. Qin, Y. Wang, T.C. Lim, Dynamic Characteristics of Motor-Gear System under Load Saltations and Voltage Transients. Mech. Syst. Signal Pr. **100**, 1-16 (2018). DOI: https://doi.org/10.1016/j.ymssp.2017.07.039

[21] W. Bai, D. Qin, Y. Wang, T.C. Lim, Dynamic Characteristic of Electromechanical Coupling Effects in Motor-Gear System. J. Sound Vib. **423**, 50-64 (2018). DOI: https://doi.org/10.1016/j.jsv.2018.02.033

[22] J. Lin, R.G. Parker, Analytical Characterization of the Unique Properties of Planetary Gear Free Vibration. J. Vib. Acoust. **121**, 316-321 (1999). DOI: https://doi.org/10.1115/1.2893982

[23] Y. Zhang, Q. Wang, H. Ma, J. Huang, C. Zhao, Dynamic Analysis of Three-Dimensional Helical Geared Rotor System with Geometric Eccentricity. J. Mech. Sci. Technol. **27** (11), 3231-3242 (2013). DOI: https://doi.org/10.1007/s12206-013-0846-8

[24] R.H. Park, Two-Reaction Theory of Synchronous Machines Generalized Method of Analysis- Part I. Trans. AIEE. **48** (03), 716-727(1929). DOI: 10.1109/T-AIEE.1929.5055275

[25] A.T. Tadeo, K.L. Cavalca, M.J. Brennan, Dynamic Characterization of a Mechanical Coupling for a Rotating Shaft. P. I. Mech. Eng. C-J Mec. **225**, 604-616 (2011). DOI: https://doi.org/10.1243/09544062JMES2214

[26] P. Dewangan, A. Parey, A. Hammami, F. Chaari, M. Haddar, Damage Detection in Wind Turbine Gearbox Using Modal Strain Energy. Eng. Fail. Anal. **107**, 104228, (2020). DOI: https://doi.org/10.1016/j.engfailanal.2019.104228

[27] S. Wei, J. Zhao, Q. Han, F. Chu, Dynamic Response Analysis on Torsional Vibrations of Wind Turbine Geared Transmission System with Uncertainty. Renew. Energ. **78**, 60-67 (2015). DOI: https://doi.org/10.1016/j.renene.2014.12.062

[28] S. Wei, Q. Han, Z. Peng, F. Chu, Dynamic Analysis of Parametrically Excited System under Uncertainties and Multi-Frequency Excitations. Mech. Syst. Signal Pr. **72-73**, 762-784 (2016). DOI: https://doi.org/10.1016/j.ymssp.2015.10.036

[29] R.G. Parker, J. Lin, Mesh Phasing Relationships in Planetary and Epicyclic Gears. ASME. J. Mech. Des. **126**, 365-370 (2004). DOI: https://doi.org/10.1115/1.1667892

[30] K. Krauze, K. Mucha, T. Wydro, R. Klempka, Assessment of the Structure of Cutting Heads with Regard to the Mining Machine Load Using Proprietary Software. Energies, **15**, 6886 (2022). DOI: https://doi.org/10.3390/en15196886

[31] Ł. Bołoz, L. F. Castañeda, Computer-Aided Support for the Rapid Creation of Parametric Models of Milling Units for Longwall Shearers. Management Systems in Production Engineering, **26** (4): 193-199 (2018). DOI: https://doi.org/10.1515/mspe-2018-0031

[32] J. Jia, Research on Theory of Sharer Drum Cutting Coal and Cutting Dynamics. Master's thesis, Taiyuan University of Technology, Taiyuan, July (2016).

[33] S. Mo, T. Zhang, G. Jin, X. Cao, H. Gao, Analytical Investigation on Load Sharing Characteristics of Herringbone Planetary Gear Train with Flexible Support and Floating Sun Gear. Mech. Mach. Theory **144**, 103670 (2020). DOI: https://doi.org/10.1016/j.mechmachtheory.2019.103670